Thermochemical Non-Equilibrium Reentry Flows in Two-Dimensions: Eleven Species Model – Part II

EDISSON SÁVIO DE GÓES MACIEL[(1)] and AMILCAR PORTO PIMENTA[(2)]
IEA – Aeronautical Engineering Division
ITA – Aeronautical Technological Institute
Praça Mal. do Ar Eduardo Gomes, 50 – Vila das Acácias – São José dos Campos – SP – 12228-900
BRAZIL
[(1)]edisavio@edissonsavio.eng.br [(1)]http://www.edissonsavio.eng.br and [(2)]amilcar@ita.br

Abstract: - This work describes the thermochemical non-equilibrium simulations of reactive flow in two-dimensions. The Van Leer and Liou and Steffen Jr. schemes, in their first- and second-order versions, are implemented to accomplish the numerical simulations. The Euler and Navier-Stokes equations, on a finite volume context and employing structured and unstructured spatial discretizations, are applied to solve the "hot gas" hypersonic flows around a blunt body, around a double ellipse, and around a reentry capsule in two-dimensions. The second-order version of the Van Leer and Liou and Steffen Jr. schemes are obtained from a "MUSCL" extrapolation procedure in a context of structured spatial discretization. In the unstructured context, only first-order solutions are presented. The convergence process is accelerated to the steady state condition through a spatially variable time step procedure, which has proved effective gains in terms of computational acceleration (Maciel). The reactive simulations involve a Earth atmosphere chemical model of eleven species: N, O, N_2, O_2, NO, N^+, O^+, N_2^+, O_2^+, NO^+ and e^-, based on the works of Dunn and Kang and of Park. Thirty-two, to the former, and fourth-three, to the latter, chemical reactions, involving dissociation, recombination and ionization, are simulated by the proposed models. The Arrhenius formula is employed to determine the reaction rates and the law of mass action is used to determine the source terms of each gas species equation. The results have indicated the Van Leer scheme as the most accurate one, both inviscid and viscous cases. This work is the second part of this study and only the solutions of the structured blunt body problem are presented.

Key-Words: - Thermochemical non-equilibrium, Earth reentry, Eleven species model, Hypersonic "hot gas" flow, Finite volume, Euler and Navier-Stokes equations, Two-dimensions.

1 Introduction

A hypersonic flight vehicle has many applications for both military and civilian purposes including reentry vehicles such as the Space Shuttle and the Automated Transfer Vehicle (ATV) of the European Space Agency (ESA). The extreme environment of a hypersonic flow has a major impact on the design and analysis of the aerodynamic and thermal loading of a reentry or hypersonic cruise vehicle. During a hypersonic flight, the species of the flow field are vibrationally excited, dissociated, and ionized because of the very strong shock wave which is created around a vehicle. Because of these phenomena, it is necessary to consider the flow to be in thermal and chemical non-equilibrium.

In high speed flows, any adjustment of chemical composition or thermodynamic equilibrium to a change in local environment requires certain time. This is because the redistribution of chemical species and internal energies require certain number of molecular collisions, and hence a certain characteristic time. Chemical non-equilibrium occurs when the characteristic time for the chemical reactions to reach local equilibrium is of the same order as the characteristic time of the fluid flow. Similarly, thermal non-equilibrium occurs when the characteristic time for translation and various internal energy modes to reach local equilibrium is of the same order as the characteristic time of the fluid flow. Since chemical and thermal changes are the results of collisions between the constituent particles, non-equilibrium effects prevail in high-speed flows in low-density air.

To a more detailed motivation of the present study, the reader is encouraged to read the first part of this study, [1].

This work, second of this study, describes a numerical tool to perform thermochemical non-equilibrium simulations of reactive flow in two-dimensions, using an eleven species chemical model. The [2-3] schemes, in their first- and second-order versions, are implemented to accomplish the numerical simulations. The Euler and Navier-Stokes equations, on a finite volume context and employing structured and unstructured spatial discretizations, are applied to solve the "hot gas" hypersonic flows

around a blunt body, around a double ellipse, and around a reentry capsule in two-dimensions. The second-order versions of the [2-3] schemes are obtained from a "MUSCL" extrapolation procedure in a context of structured spatial discretization. In terms of unstructured spatial discretization, only first-order solutions are presented. The convergence process is accelerated to the steady state condition through a spatially variable time step procedure, which has proved effective gains in terms of computational acceleration (see [4-5]). In this paper, the blunt body structured solutions are shown.

The reactive simulations involve an air chemical model of eleven species: N, O, N_2, O_2, NO, N^+, O^+, N_2^+, O_2^+, NO^+ and e^-. Thirty-two (32) or Fourth-three (43) chemical reactions, involving dissociation, recombination and ionization, are simulated by the proposed models of [6-7], respectively. The Arrhenius formula is employed to determine the reaction rates and the law of mass action is used to determine the source terms of each gas species equation.

2 Results

The initial condition to the blunt body problem is described in Tab. 1. The freestrem Mach number is 8.78 and the blunt body reentry speed is near 4,800 m/s. The flight altitude is 40,000 m.

Table 1 Initial conditions to the problem of the blunt body.

Property	Value
M_∞	8.78
ρ_∞	0.00326 kg/m^3
p_∞	687 Pa
U_∞	4,776 m/s
T_∞	694 K
$T_{v,\infty}$	694 K
Altitude	40,000 m
c_N	10^{-9}
c_O	0.07955
c_{O_2}	0.13400
c_{NO}	0.05090
c_{N+}	0.0
c_{O+}	0.0
c_{N2+}	0.0
c_{O2+}	0.0
c_{NO+}	0.0
c_{e-}	0.0
L	2.0 m
Re_∞	2.3885x10^6

2.1. Dunn and Kang incomplete model

2.1.1. Structured, inviscid and first-order solutions

Figures 1 and 2 exhibit the pressure contours obtained by the [2-3] schemes as using the [6] chemical model and the incomplete version of the 11 (eleven) species formulation. As can be seen, the [3] pressure field is more severe than the [2] pressure field. This aspect characterizes the [3] scheme as more conservative than the [2] scheme. Good symmetry properties are observed in both solutions. No oscillations in the solutions are observed.

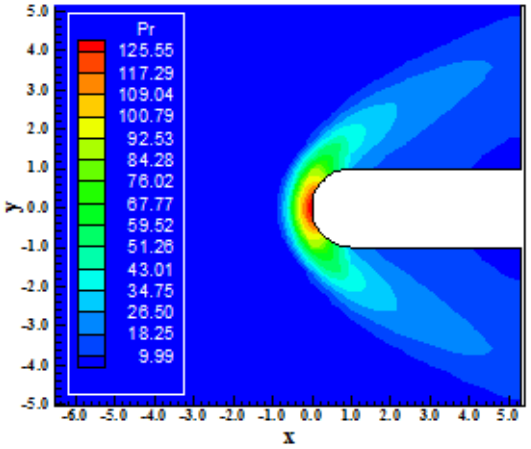

Figure 1. Pressure contours (DK-VL).

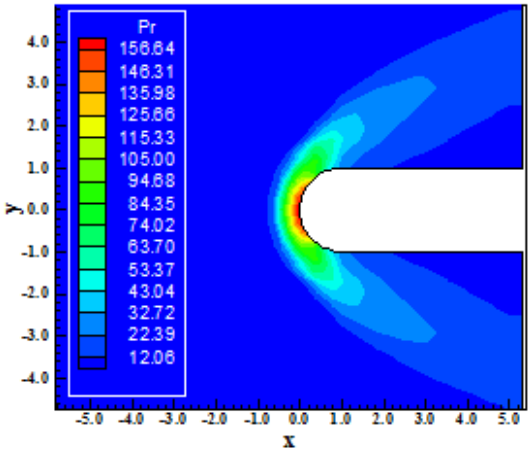

Figure 2. Pressure contours (DK-LS).

Figures 3 and 4 show the Mach number contours obtained by the [2] and by the [3] schemes as using the [6] chemical model. The incomplete eleven species formulation is employed. The Mach number field is practically the same. The [2] solution presents a smoother behavior than the [3] solution. The shock wave presents the expected behavior:

normal shock at the stagnation region, oblique shock along the body and Mach wave at the far field.

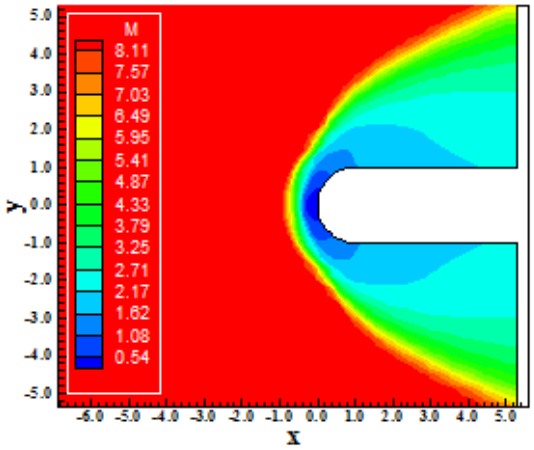

Figure 3. Mach number contours (DK-VL).

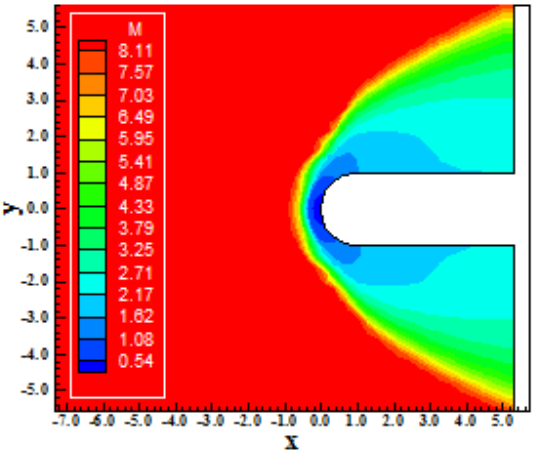

Figure 4. Mach number contours (DK-LS).

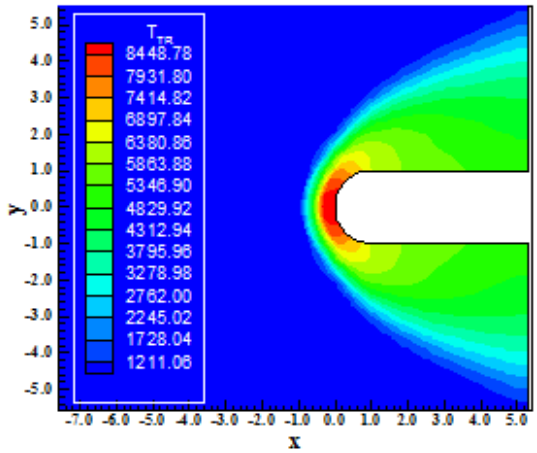

Figure 5. Translational/rotational temperature contours (DK-VL).

Figures 5 and 6 exhibit the translational / rotational temperature contours obtained by the [2-3] schemes, using the [6] chemical model. As can be observed, the most severe temperature field is obtained by the [2] scheme. Good symmetry properties are observed.

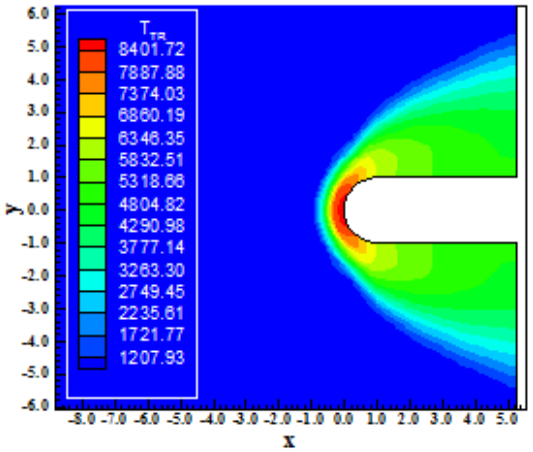

Figure 6. Translational/rotational temperature contours (DK-LS).

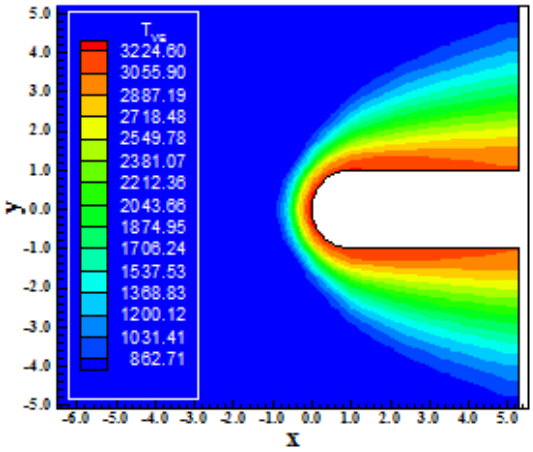

Figure 7. Vibrational temperature contours (DK-VL).

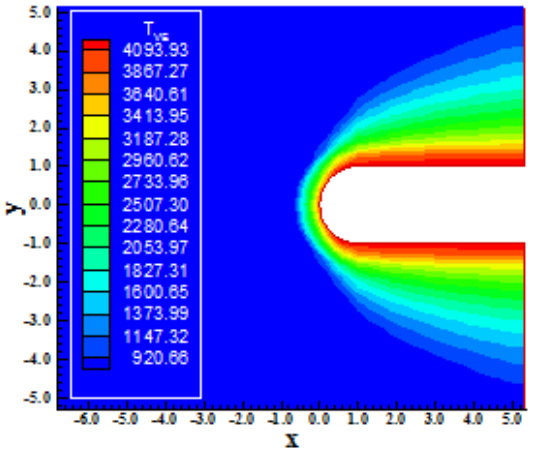

Figure 8. Vibrational temperature contours (DK-LS).

Figures 7 and 8 exhibit the vibrational temperature field, whence the [3] vibrational

temperature field is more severe. Figure 9 and 10 show the mass fraction distributions of the eleven species obtained by the [2-3] schemes. Good formation of NO resulting from good dissociation of N_2 and O_2. The formation of O is also highlighted.

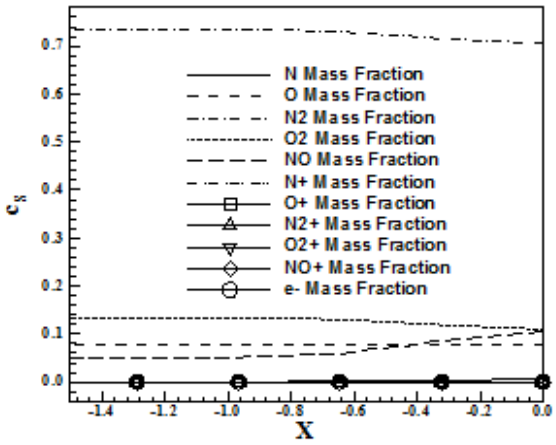

Figure 9. Species mass fraction along the stagnation line (DK-VL).

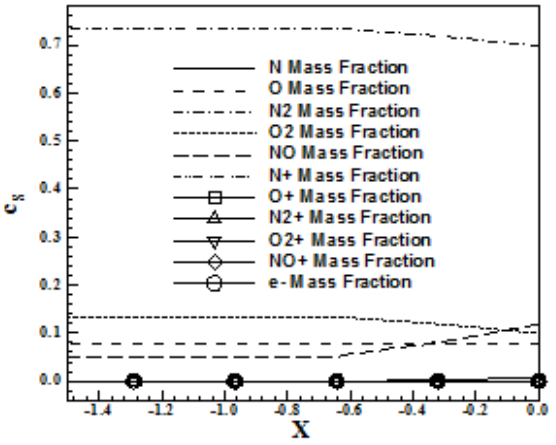

Figure 10. Species mass fraction along the stagnation line (DK-LS).

2.1.2. Structured, viscous and first-order solutions

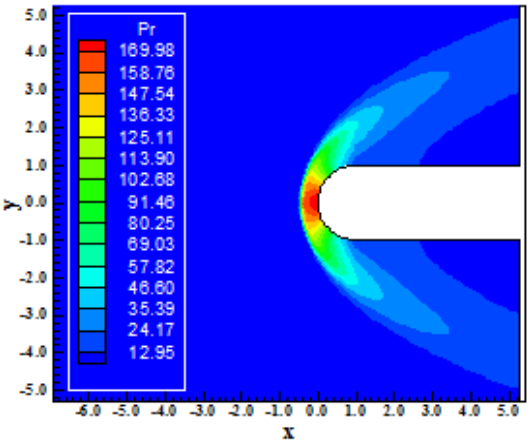

Figure 11. Pressure contours (DK-VL).

Figures 11 and 12 exhibit the pressure contours obtained by the [2-3] schemes, using the [6] chemical model, in a viscous, first order formulation. The most severe pressure field is obtained by [2] solution, with opposed behavior of the inviscid solution. Good symmetry properties are observed in both solutions.

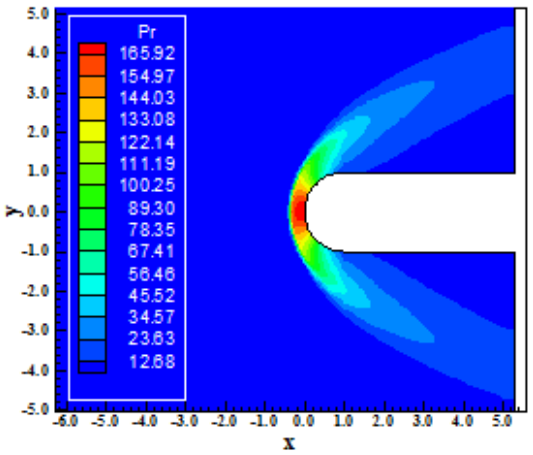

Figure 12. Pressure contours (DK-LS).

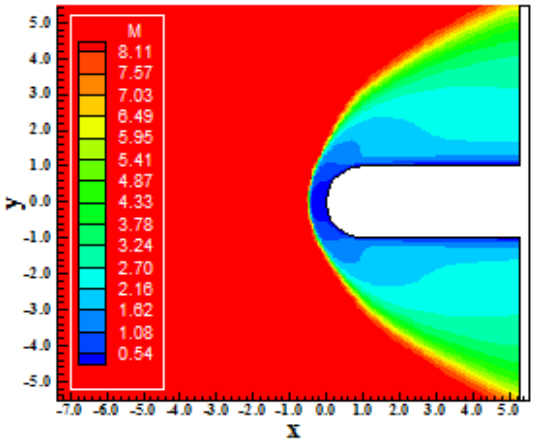

Figure 13. Mach number contours (DK-VL).

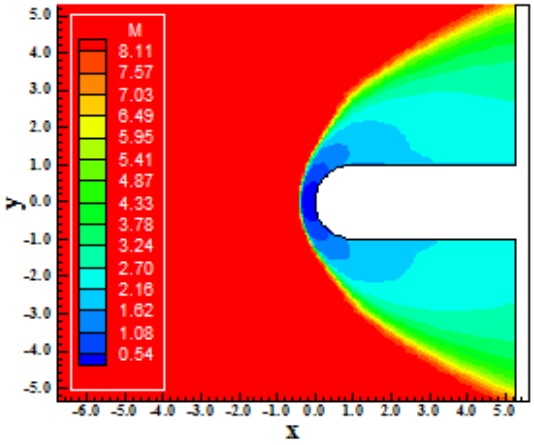

Figure 14. Mach number contours (DK-LS).

In Figures 13 and 14 are presented the Mach number contours obtained by the [2-3] schemes, in this viscous formulation. The shock is well captured. The shock wave pursues the main aspects of a shock structure: normal shock, oblique shock and Mach wave.

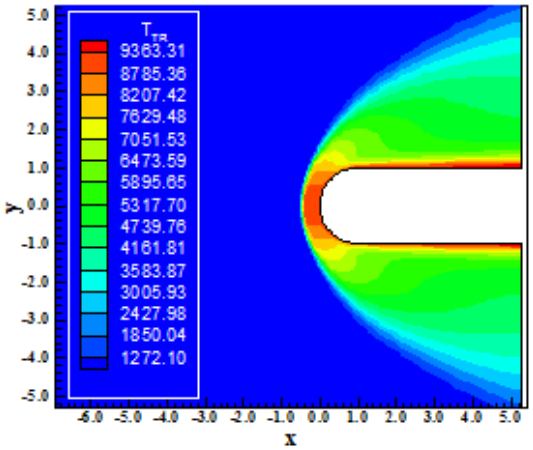

Figure 15. Translational/rotational temperature contours (DK-VL).

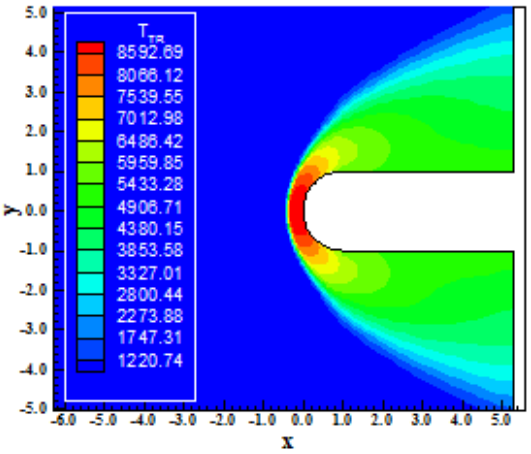

Figure 16. Translational/rotational temperature contours (DK-LS).

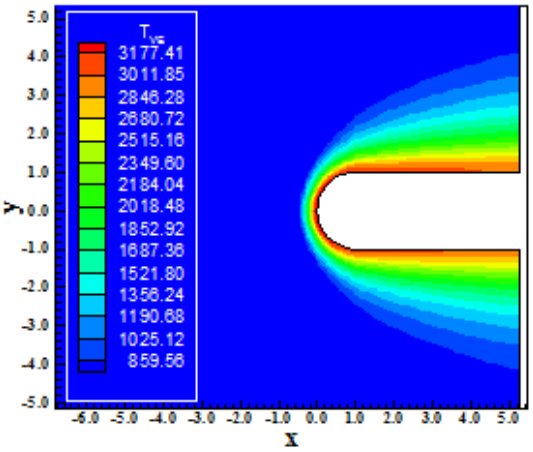

Figure 17. Vibrational temperature contours (DK-VL).

Figures 15 and 16 show the translational / rotational temperature fields captured by the [2-3] algorithms. The [2] solution presents more severe temperature field than the [3] solution. The [2] temperature field is distributed along the body geometry, whereas the [3] solution is distributed closer to the nose's blunt body.

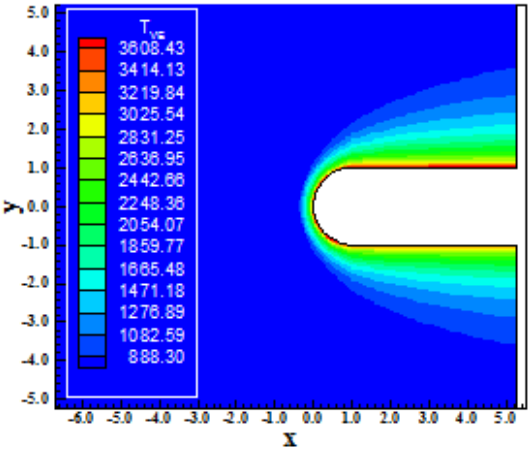

Figure 18. Vibrational temperature contours (DK-LS).

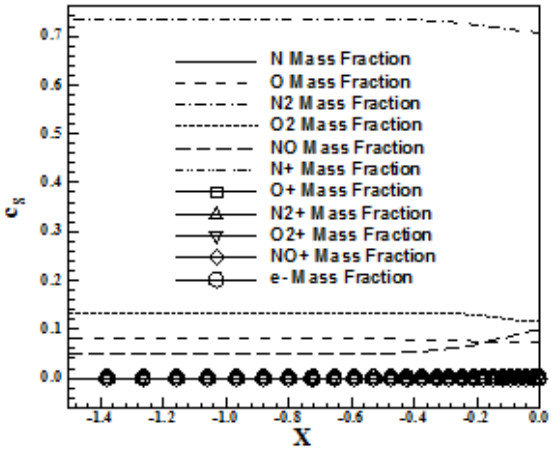

Figure 19. Species mass fraction along the stagnation line (DK-VL).

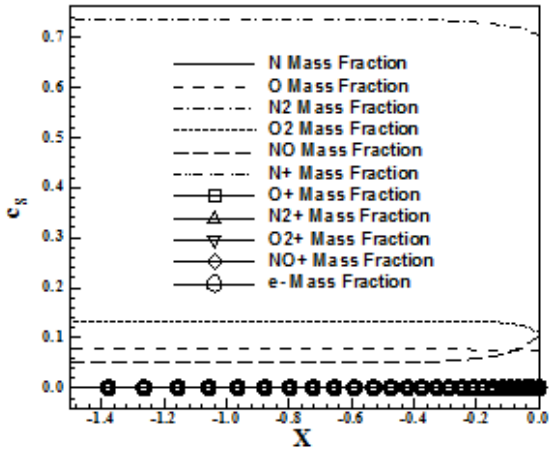

Figure 20. Species mass fraction along the stagnation line (DK-LS).

Figures 17 and 18 present the vibrational temperature field. The vibrational temperature contours is more critical in the [3] solution. A small boundary layer is formed close to the wall and, considering the Reynolds number, is turbulent. The implementation of a turbulent model is the next step in this work, aiming to verify the characteristic of such flow. Figures 19 and 20 exhibit the mass fraction distributions of the eleven species along the stagnation line. Good formations of NO and O, due to the N_2 and O_2 dissociations.

2.1.3. Structured, inviscid and second-order solutions

Figures 21 and 22 show the pressure contours to the second order accuracy of the numerical algorithms of [2] and [3], in the solution of the inviscid flow and the use of the [6] chemical model. The [2-3] solutions present concrete differences, being the [3] solution more strength and conservative.

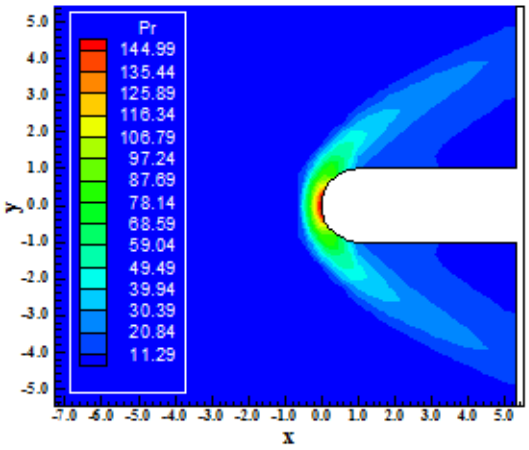

Figure 21. Pressure contours (DK-VL).

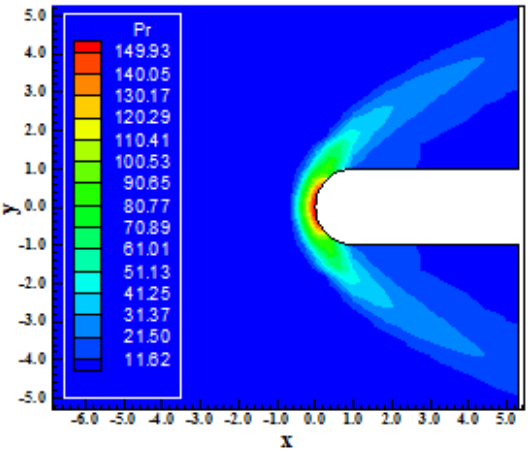

Figure 22. Pressure contours (DK-LS).

Figures 23 and 24 present the Mach number fields obtained by the [2-3] schemes, as using the [6] chemical model and an eleven species formulation. The Mach number fields are basically the same.

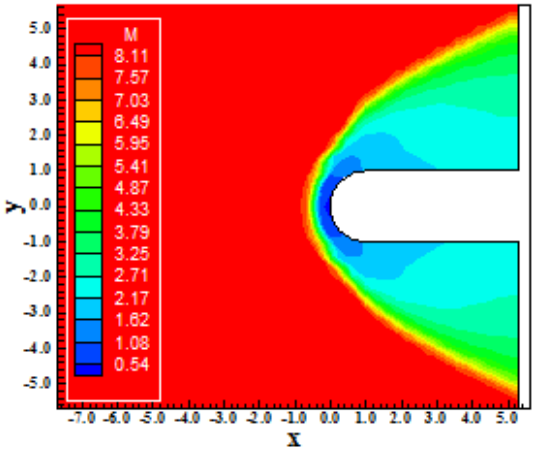

Figure 23. Mach number contours (DK-VL).

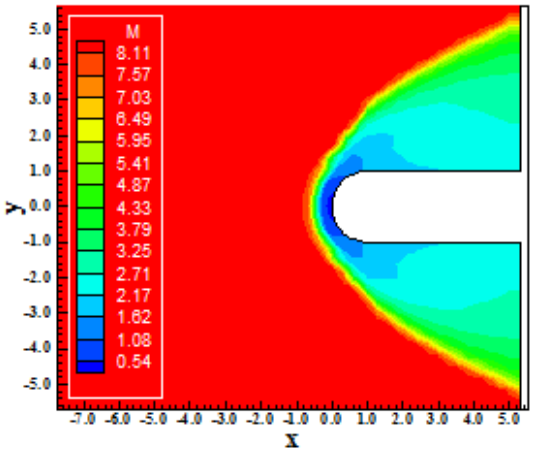

Figure 24. Mach number contours (DK-LS).

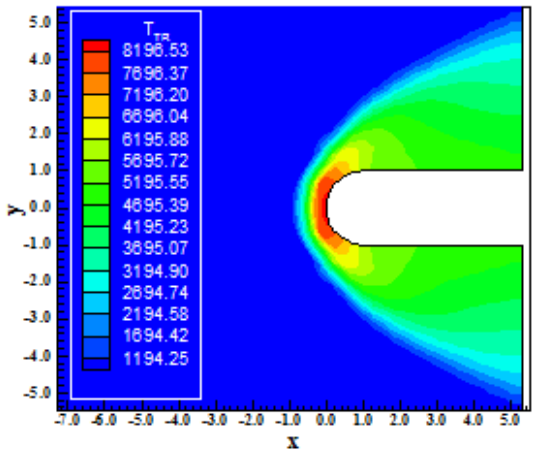

Figure 25. Translational/rotational temperature contours (DK-VL).

Figures 25 and 26 show the translational / rotational temperature contours around the blunt body, captured by the [2-3] algorithms. The translational/rotational temperature peak is more severe in the [3] solution, ratifying the more conservative behavior of [3].

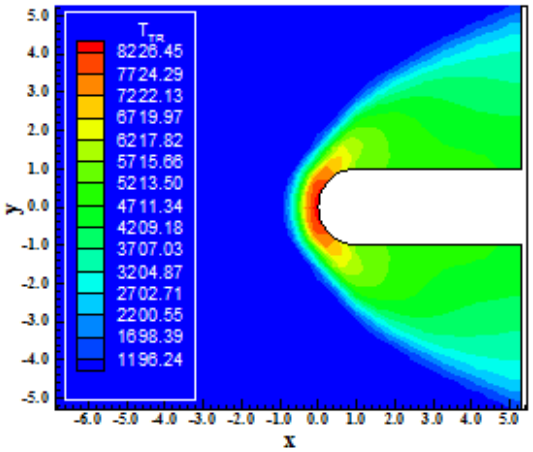

Figure 26. Translational/rotational temperature contours (DK-LS).

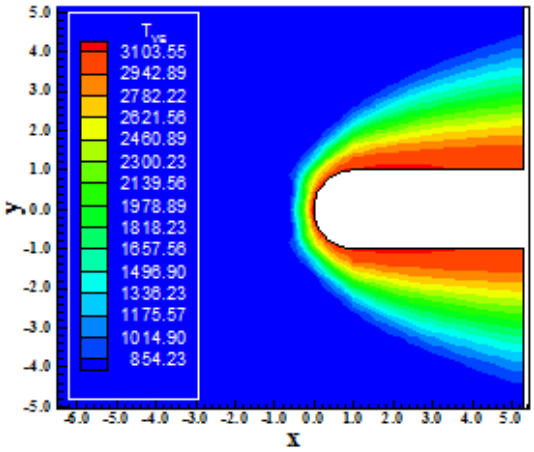

Figure 27. Vibrational temperature contours (DK-VL).

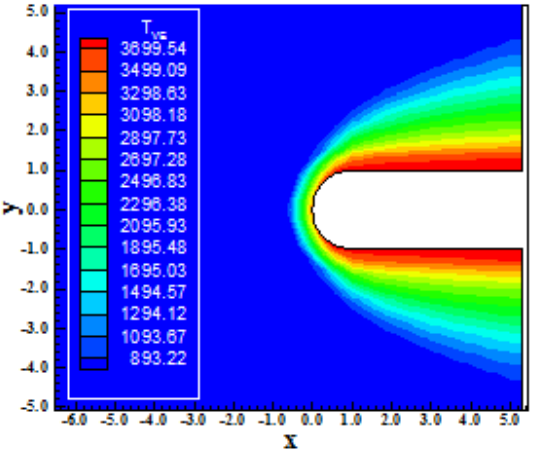

Figure 28. Vibrational temperature contours (DK-LS).

Figures 27 and 28 exhibit the vibrational temperature contours obtained by [2-3] numerical algorithms. The more intense temperature peak is reached by the [3] scheme, corroborating the more conservative aspect of this algorithm.

Figures 29 and 30 show the species mass fraction distributions along the stagnation line calculated by the [2-3] algorithms. Good formation of NO is observed due to dissociation of N_2 and O_2.

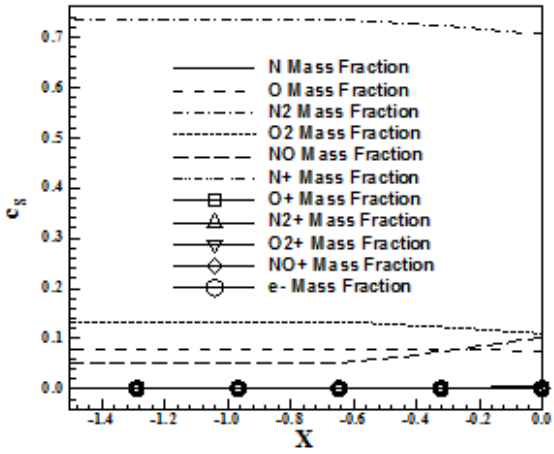

Figure 29. Species mass fraction along the stagnation line (DK-VL).

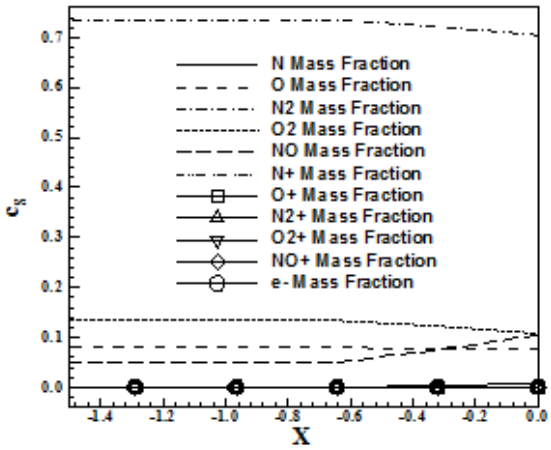

Figure 30. Species mass fraction along the stagnation line (DK-LS).

2.1.4. Structured, viscous and second-order solutions

Figures 31 and 32 exhibit the pressure contours generated by the [2-3] schemes, as using the [6] chemical model and the incomplete eleven species formulation, to the second order viscous case. The [2] scheme presents stronger pressure field than the [3] scheme. Good symmetry properties are observed.

Figures 33 and 34 show the Mach number fields captured by the [2-3] schemes. The [2] solution presents subsonic regions of flow close to the wall, whereas the [3] solution doesn't do.

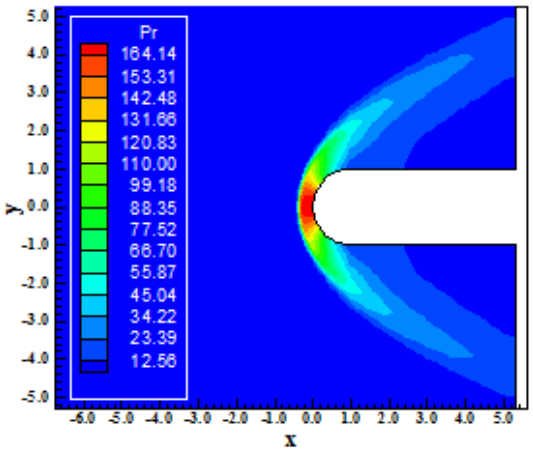

Figure 31. Pressure contours (DK-VL).

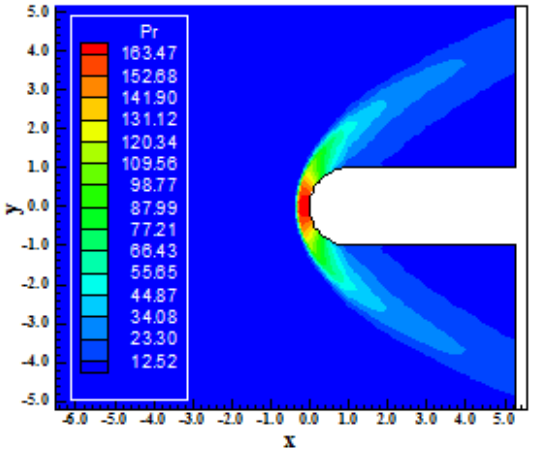

Figure 32. Pressure contours (DK-LS).

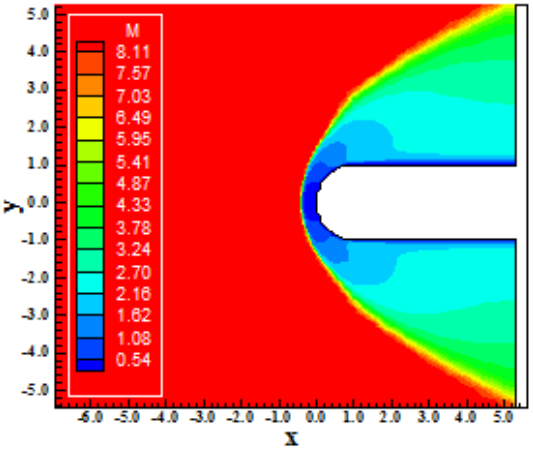

Figure 33. Mach number contours (DK-VL).

Figures 35 and 36 present the translational / rotational temperature fields obtained by the [2-3] schemes, using the [6] chemical model and a viscous second-order formulation. Close to the wall the temperatures are at the range of 6,500 K detected by the [2] scheme, whereas for the [3] scheme are at the range of 5,400 K.

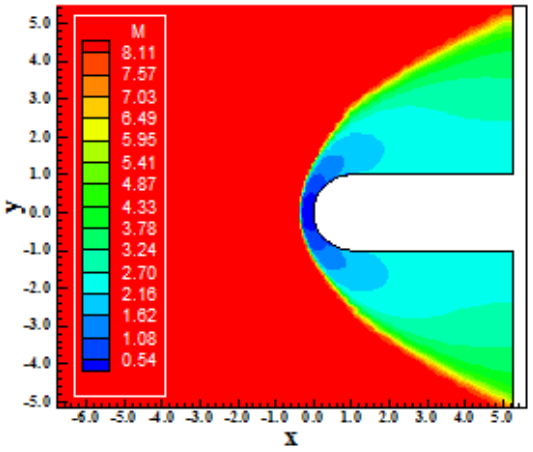

Figure 34. Mach number contours (DK-LS).

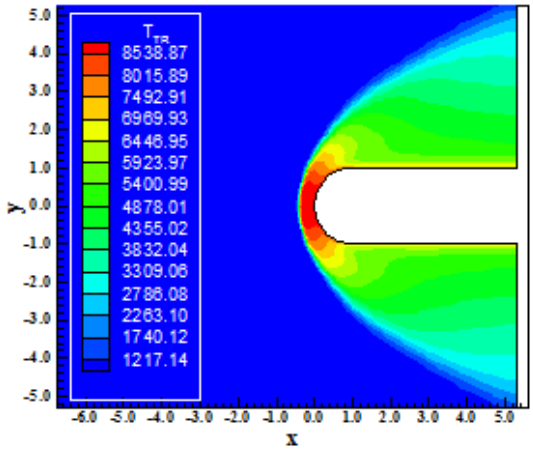

Figure 35. Translational/rotational temperature contours (DK-VL).

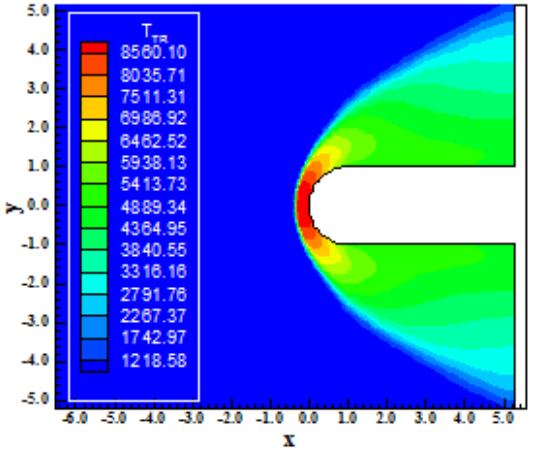

Figure 36. Translational/rotational temperature contours (DK-LS).

Figures 37 and 38 exhibit the vibrational temperature contours, which describes the behavior of the molecules vibrational excited. Figures 39 and

40 show the mass fraction distributions along the stagnation line, observed by the [2-3] algorithms.

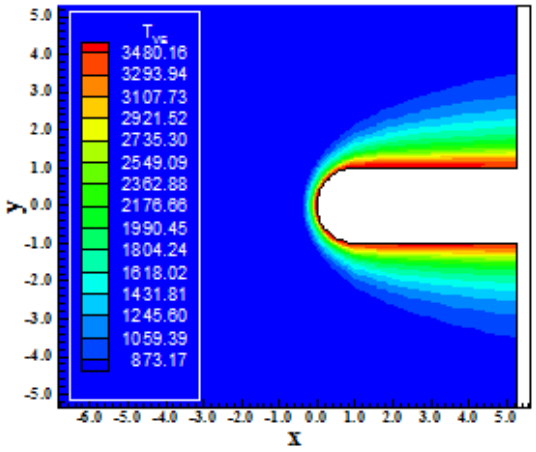

Figure 37. Vibrational temperature contours (DK-VL).

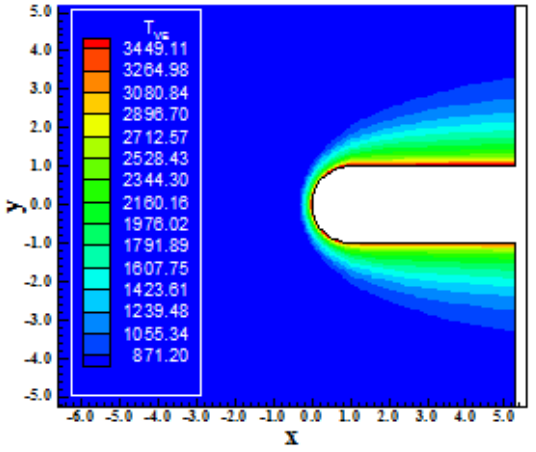

Figure 38. Vibrational temperature contours (DK-LS).

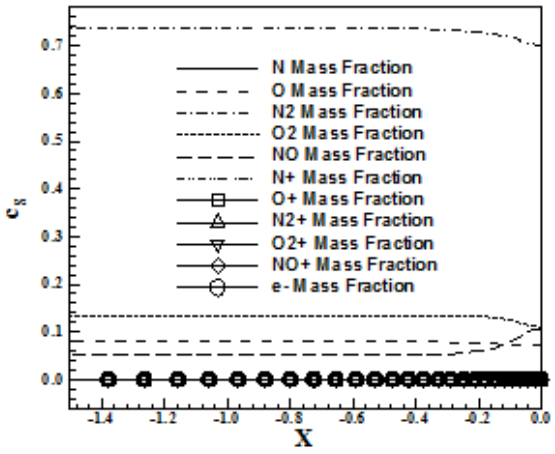

Figure 39. Species mass fraction along the stagnation line (DK-VL).

Good formation of NO is observed, conjunctly with the N_2 and O_2 dissociations. As can be observed, O is also reducing to the NO formation. This feature is observed in both algorithms.

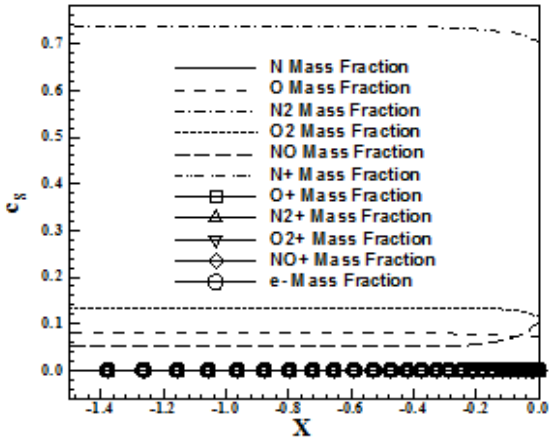

Figure 40. Species mass fraction along the stagnation line (DK-LS).

2.2. Park incomplete model

2.2.1. Structured, inviscid and first-order solutions

Figures 41 and 42 present the pressure contours obtained by the [2-3] algorithms.

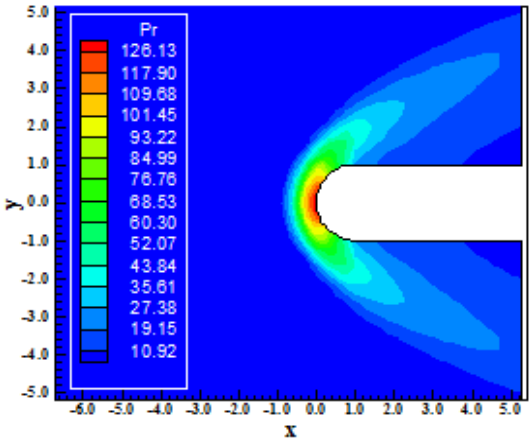

Figure 41. Pressure contours (P-VL).

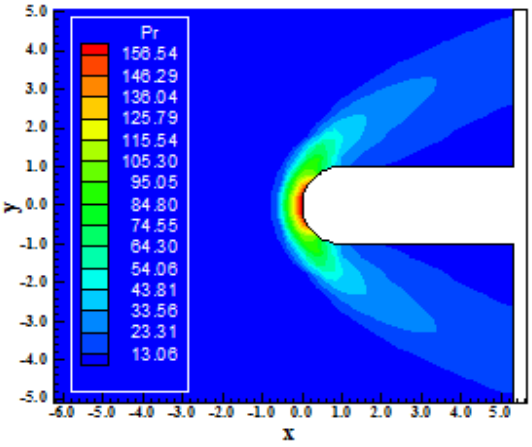

Figure 42. Pressure contours (P-LS).

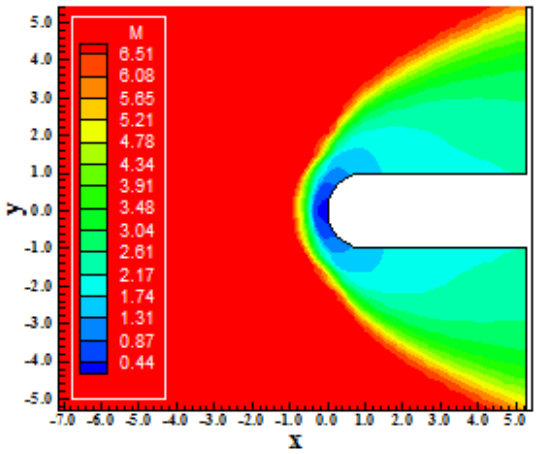

Figure 43. Mach number contours (P-VL).

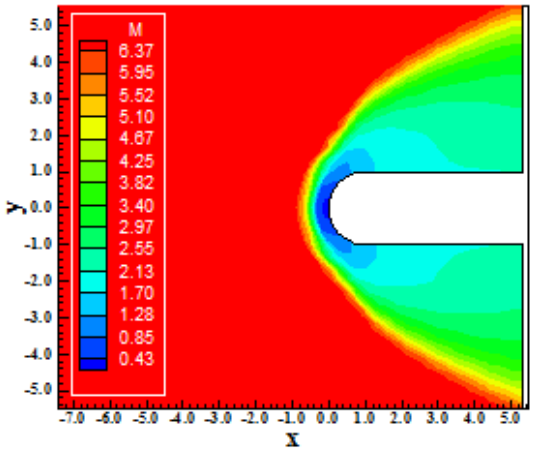

Figure 44. Mach number contours (P-LS).

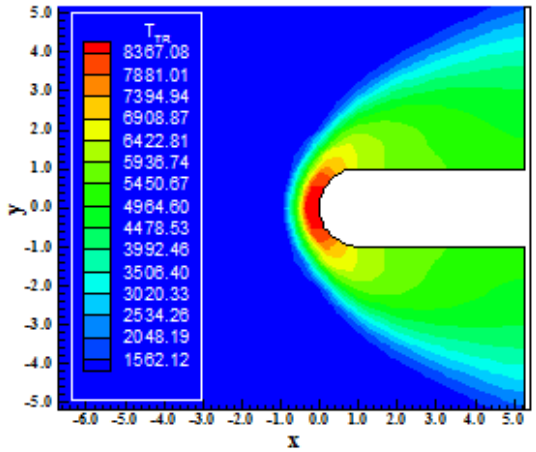

Figure 45. Translational/rotational temperature contours (P-VL).

They were generated using the [7] chemical model and the incomplete eleven species formulation. The [3] solution is stronger than the [2] solution, highlighting its more conservative characteristic. Figures 43 and 44 show the Mach number distributions around the blunt body geometry. Both Mach number fields are basically the same. The shock wave develops naturally: normal shock, oblique shock, and Mach wave.

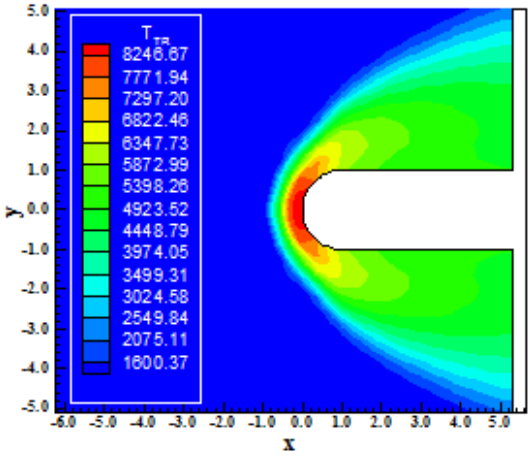

Figure 46. Translational/rotational temperature contours (P-LS).

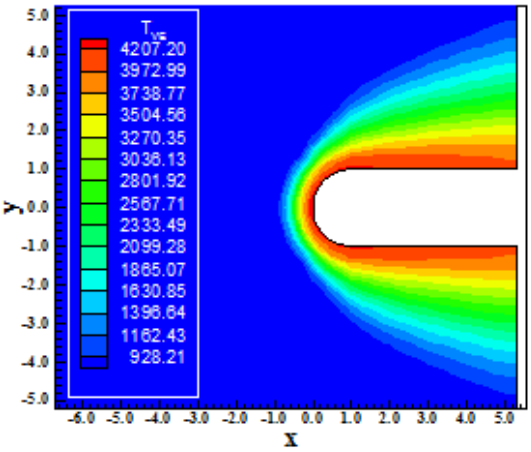

Figure 47. Vibrational temperature contours (P-VL).

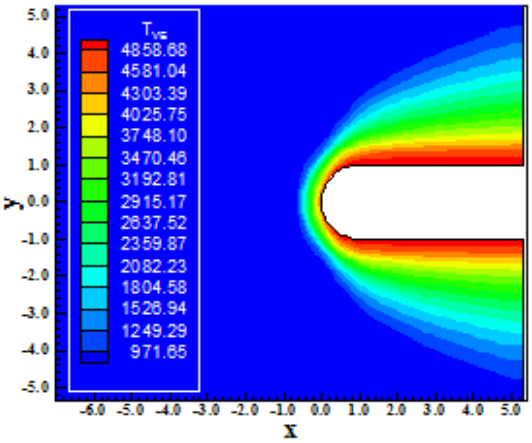

Figure 48. Vibrational temperature contours (P-LS).

As important difference between the [6] and [7] chemical models, the Mach number peak of the [7]

model is lower than the respective peak of the [6] model. It was a characteristic observed in all solutions presented in this work.

Figure 45 and 46 show the translational / rotational temperature contours around the blunt body geometry. The more intense translational / rotational field is detected by the [2] solution. Figures 47 and 48 highlight the vibrational temperature contours, with the [3] scheme presenting the most intense field.

Figure 49 and 50 show the species mass fraction distributions along the stagnation line. Both schemes present accentuate formation of NO and O, as well of N. Dissociations of N_2 and O_2 are the main responsible by such formations.

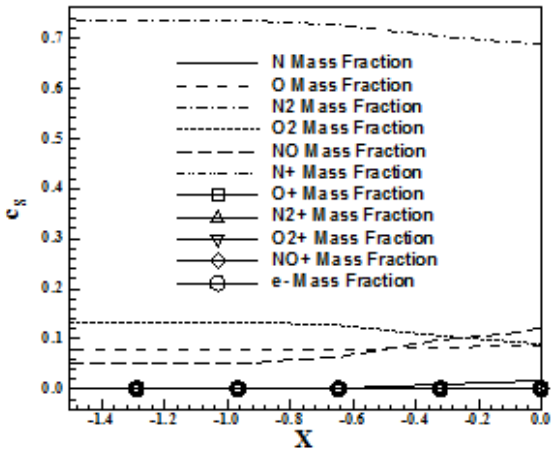

Figure 49. Species mass fraction along the stagnation line (P-VL).

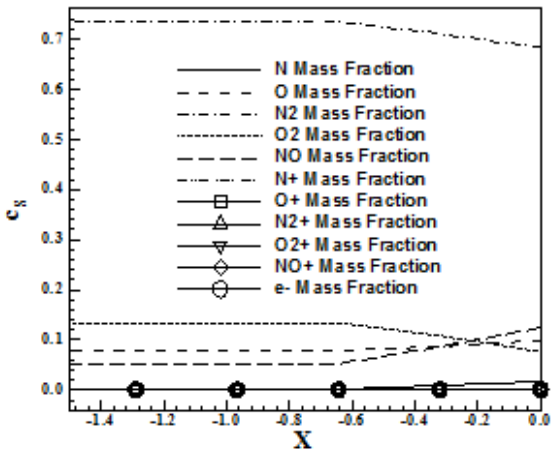

Figure 50. Species mass fraction along the stagnation line (P-LS).

2.2.2. Structured, viscous and first-order solutions

Figures 51 and 52 present the pressure contours obtained by the [2-3] numerical algorithms as using the [7] chemical model, in an incomplete eleven species formulation, in treating viscous flows. The [2] pressure contours are more severe than the [3] pressure contours. Good symmetry is observed in the figures.

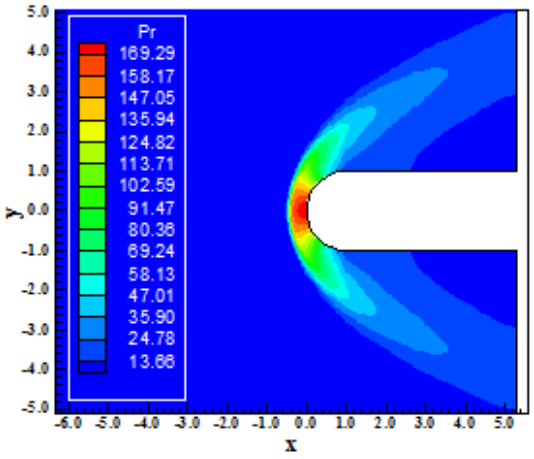

Figure 51. Pressure contours (P-VL).

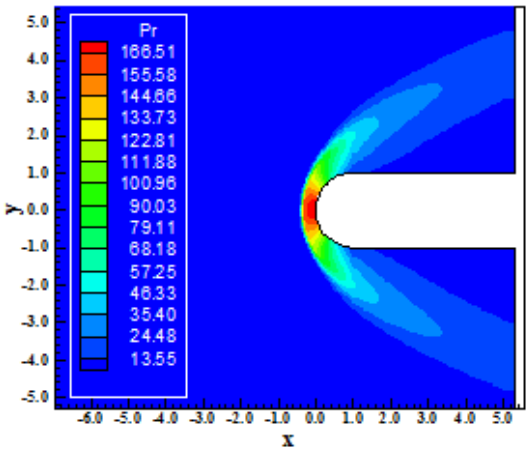

Figure 52. Pressure contours (P-LS).

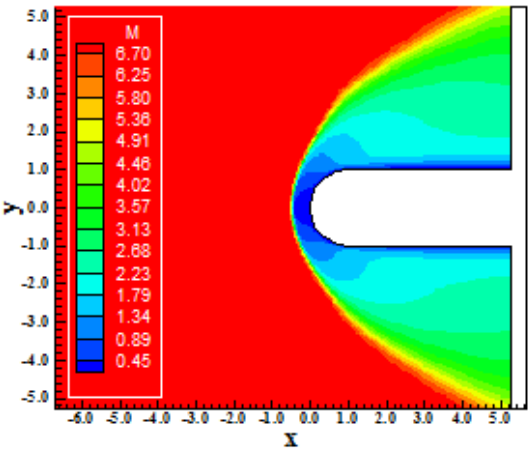

Figure 53. Mach number contours (P-VL).

Figures 53 and 54 show the Mach number contours obtained by the [2] and by the [3] algorithms as using the [7] chemical model and an

incomplete eleven species formulation. The more intense Mach number field is due to [2]. A region of subsonic flow is formed at the body wall in the [2] solution. The [3] solution did not present such behavior.

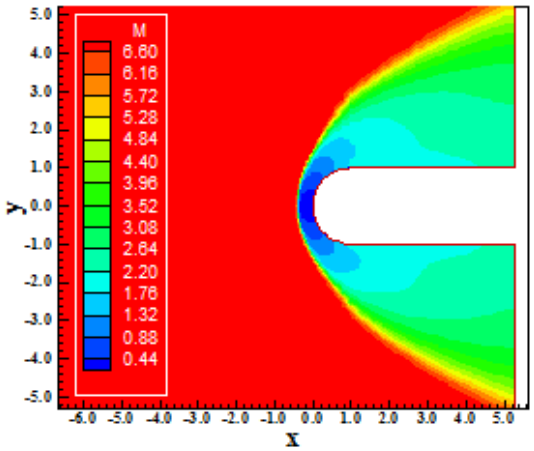

Figure 54. Mach number contours (P-LS).

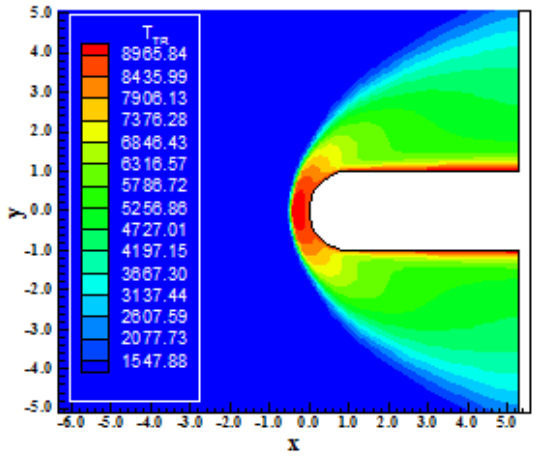

Figure 55. Translational/rotational temperature contours (P-VL).

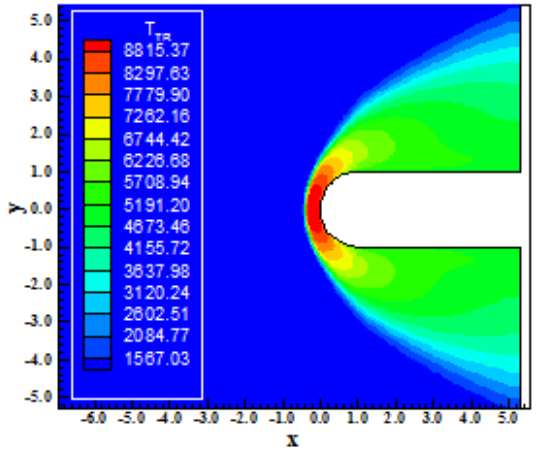

Figure 56. Translational/rotational temperature contours (P-LS).

Figures 55 and 56 exhibit the translational / rotational temperature contours obtained by the [2] and by the [3] schemes. As can be seen, the [2] solution presents a more severe temperature field. Figures 57 and 58 show the vibrational temperature contours obtained by the [2] and by the [3] numerical schemes. The most intense is due to [3].

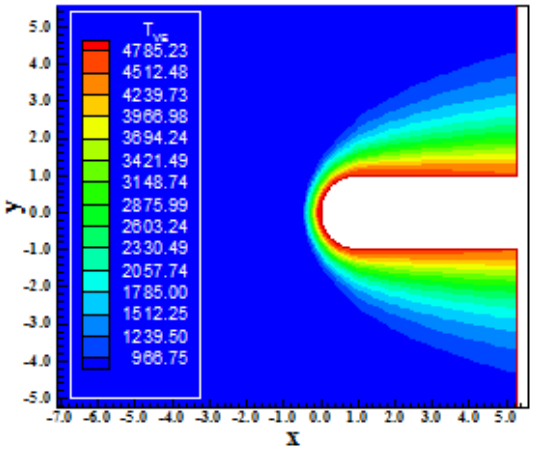

Figure 57. Vibrational temperature contours (P-VL).

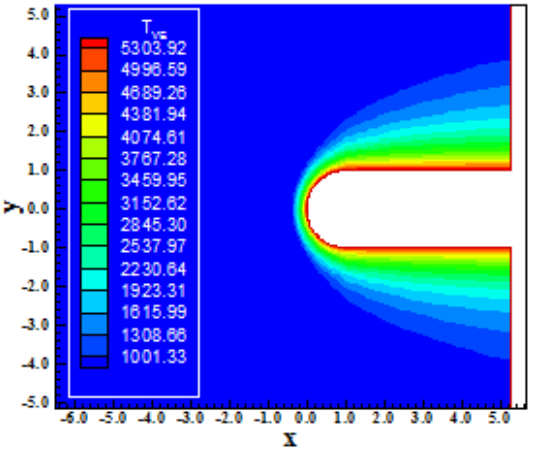

Figure 58. Vibrational temperature contours (P-LS).

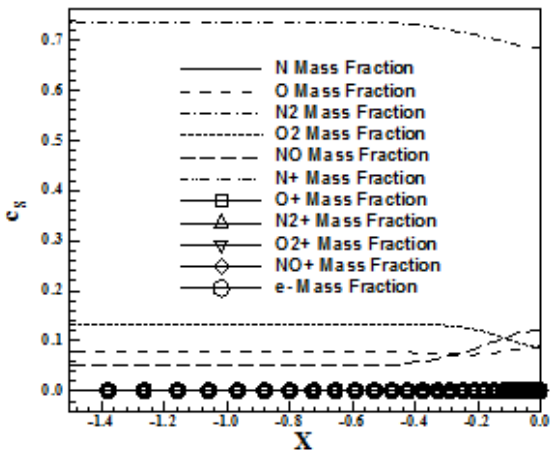

Figure 59. Species mass fraction along the stagnation line (P-VL).

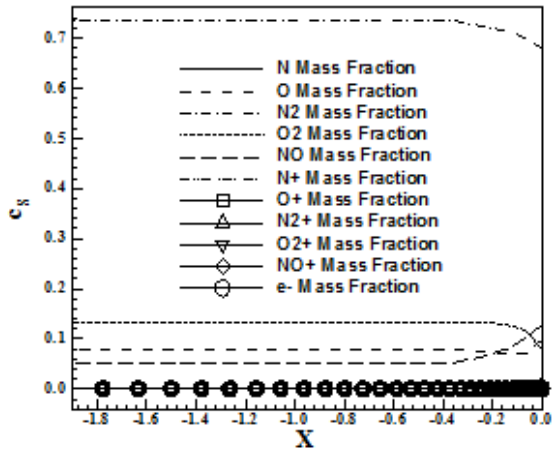

Figure 60. Species mass fraction along the stagnation line (P-LS).

Figures 59 and 60 present the species mass fraction distributions along the stagnation line obtained by the [2] and by the [3] schemes. Good formation of NO is observed, with consequently decrease in the N_2 and O_2.

2.2.3. Structured, inviscid and second-order solutions

Figures 61 and 62 exhibit the pressure contours obtained by the [2] and by the [3] algorithms, respectively. The pressure field generated by the [3] scheme is more severe than that generated by the [2] scheme. Good symmetry properties are observed.

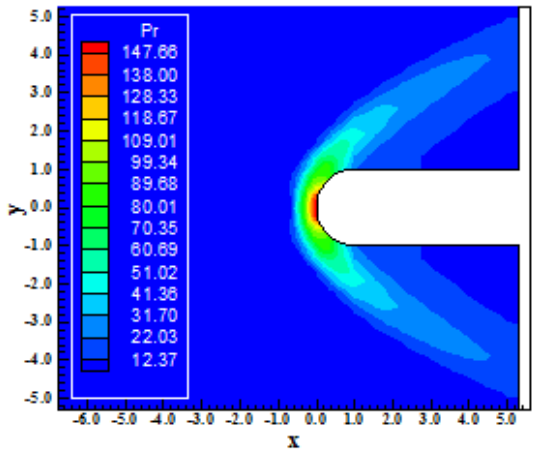

Figure 61. Pressure contours (P-VL).

Figures 63 and 64 show the Mach number contours obtained by the [2] and the [3] schemes, respectively. They were obtained using the [7] chemical model and the incomplete eleven species formulation to the inviscid case. The Mach number field obtained by the [2] scheme is more intense than that obtained by the [3] scheme. In qualitative terms, both solutions are very similar. Good symmetry properties are observed. The shock wave presents the expected behavior.

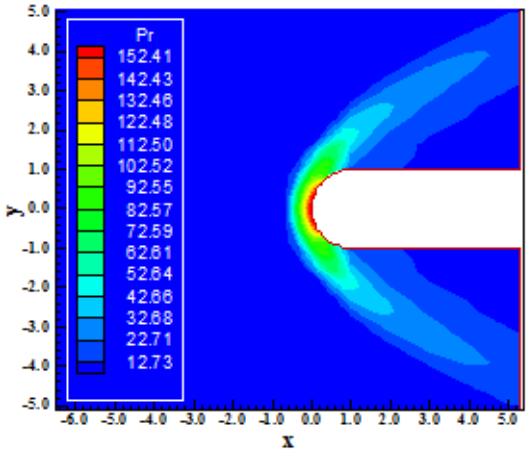

Figure 62. Pressure contours (P-LS).

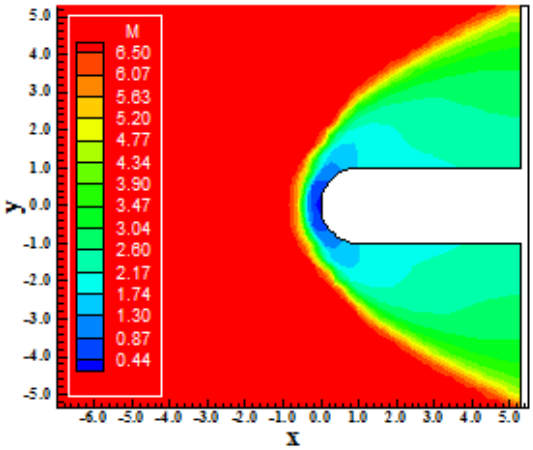

Figure 63. Mach number contours (P-VL).

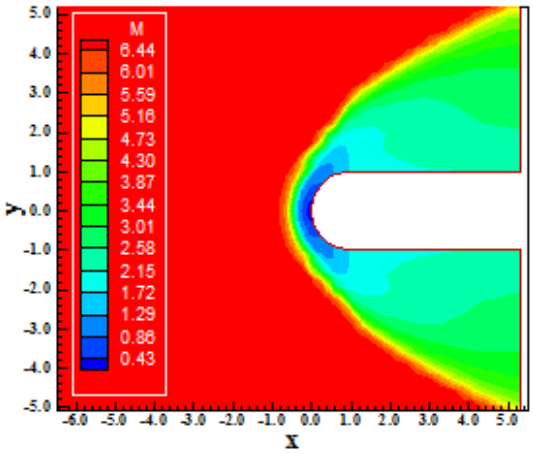

Figure 64. Mach number contours (P-LS).

Figures 65 and 66 exhibit the translational / rotational temperature contours obtained by the [2] and by the [3] numerical schemes. The most intense

translational/rotational temperature field is due to [3] algorithm. Figures 67 and 68 show the vibrational temperature contours generated by the [2-3] schemes, respectively. The most intense vibrational temperature field is due to [2], highlighting that the vibrational modes are excited.

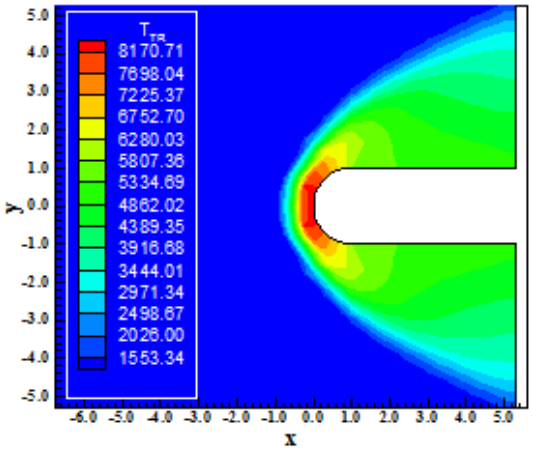

Figure 65. Translational/rotational temperature contours (P-VL).

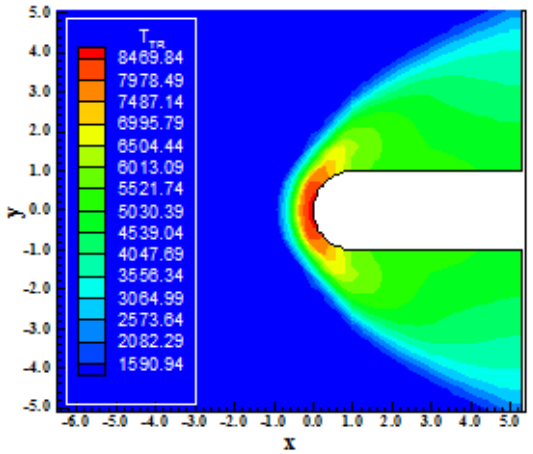

Figure 66. Translational/rotational temperature contours (P-LS).

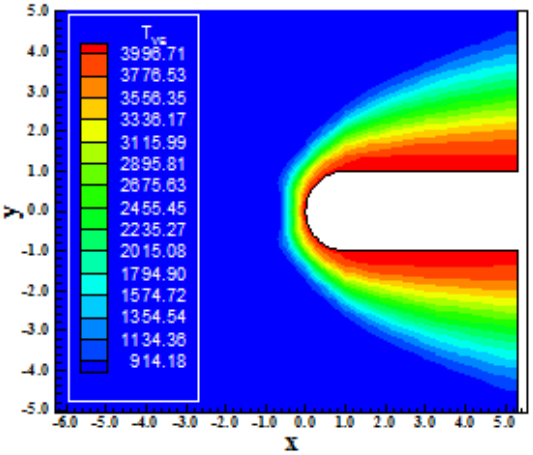

Figure 67. Vibrational temperature contours (P-VL).

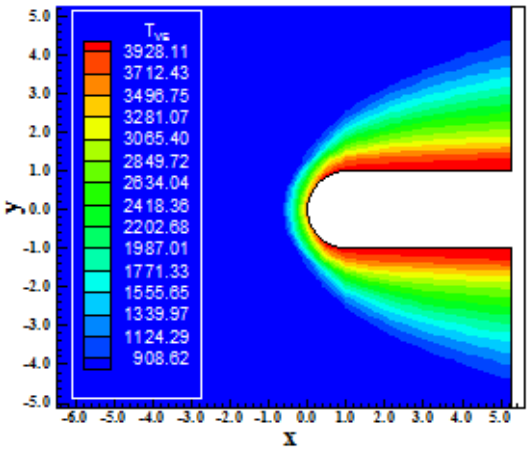

Figure 68. Vibrational temperature contours (P-LS).

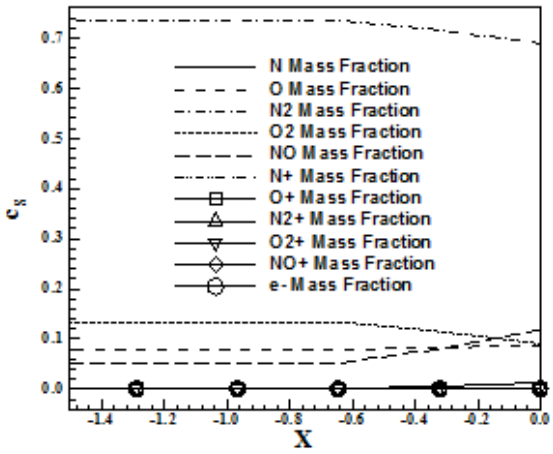

Figure 69. Species mass fraction along the stagnation line (P-VL).

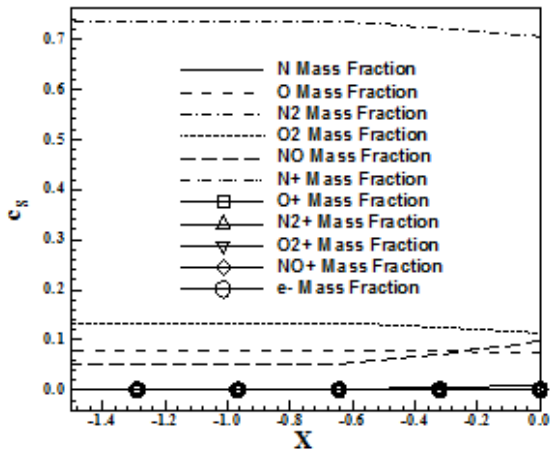

Figure 70. Species mass fraction along the stagnation line (P-LS).

Figures 69 and 70 show the species mass fraction distributions along the stagnation line generated by both algorithms. Both solutions present good formation of NO and O, with significant dissociation of N_2 and O_2. The N is weakling formed.

2.2.4. Structured, viscous and second-order solutions

Figures 71 and 72 exhibit the pressure contours generated by the [2-3] schemes, respectively, in a viscous, second-order simulation. The pressure contours generated by the [2] scheme is slightly stronger than the respective generated by the [3] scheme. Good symmetry properties are observed.

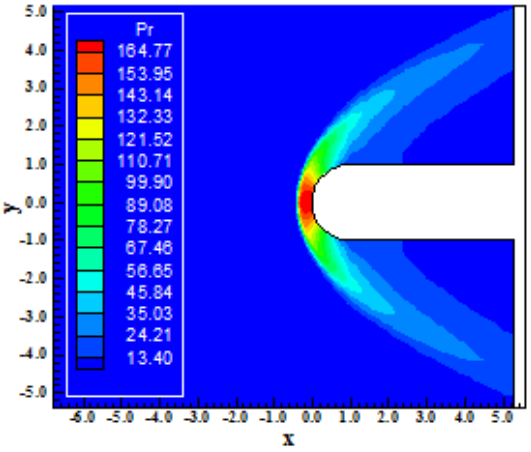

Figure 71. Pressure contours (P-VL).

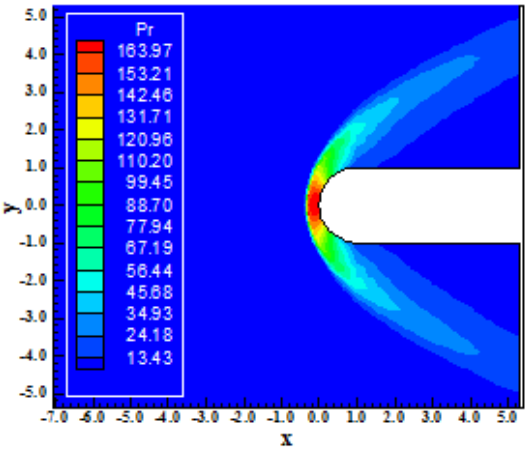

Figure 72. Pressure contours (P-LS).

Figures 73 and 74 show the Mach number field generated by the [2-3] schemes, respectively. The [2] solution presents a subsonic region formed close to the body wall, whereas the [3] solution presents a discrete subsonic region also close to the body's surface. Moreover, the [2] solution is more intense than the [3] solution. Good symmetry properties are noted. The peak of Mach number is inferior to that of the freestream, suggesting that the Park's model presents an excessive dissipation of the Mach number field.

Figures 75 and 76 present the translational / rotational temperature fields generated by the [2-3] schemes. The most intense is due to [3]. Good symmetry properties are observed in both solutions.

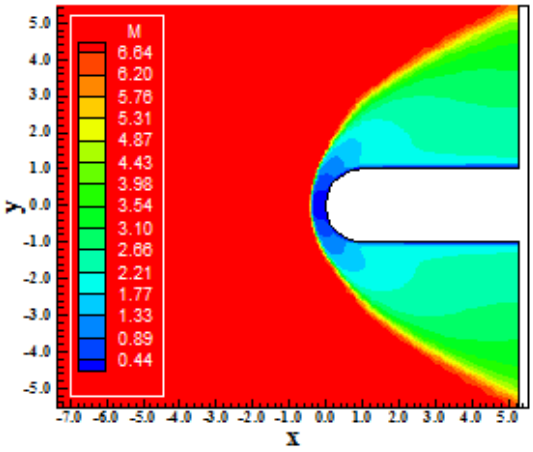

Figure 73. Mach number contours (P-VL).

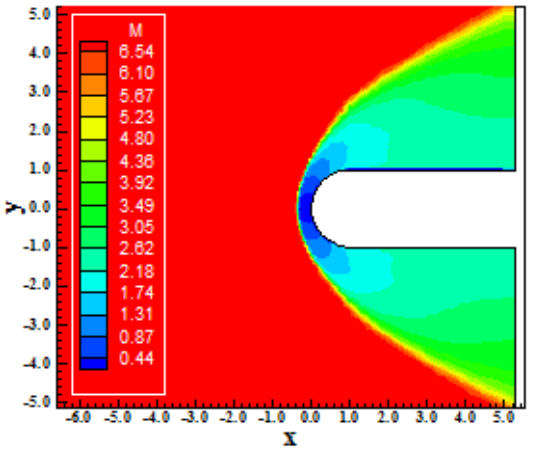

Figure 74. Mach number contours (P-LS).

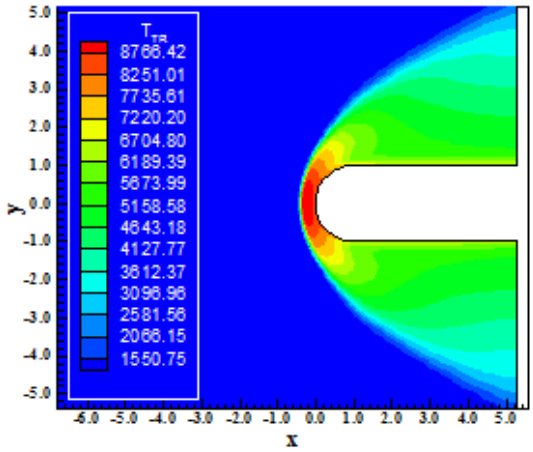

Figure 75. Translational/rotational temperature contours (P-VL).

Figures 77 and 78 exhibit the vibrational temperature contours obtained by the [2] and by the [3] numerical algorithms. The [3] solution presents a

more severe vibrational temperature field than the [2] solution.

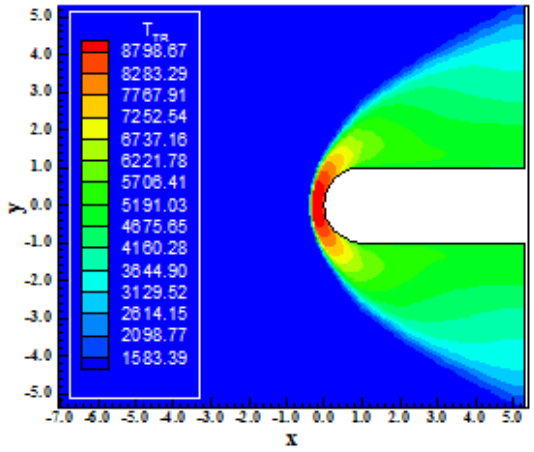

Figure 76. Translational/rotational temperature contours (P-LS).

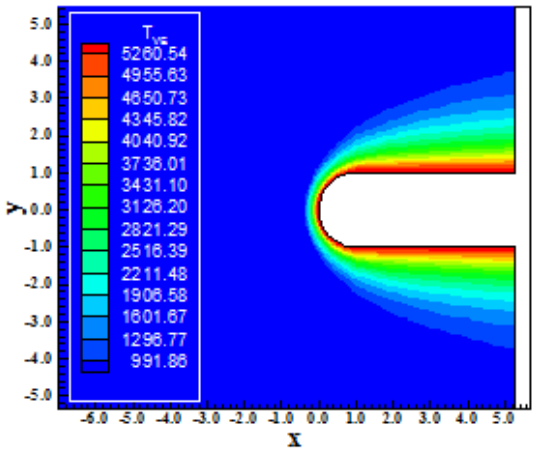

Figure 77. Vibrational temperature contours (P-VL).

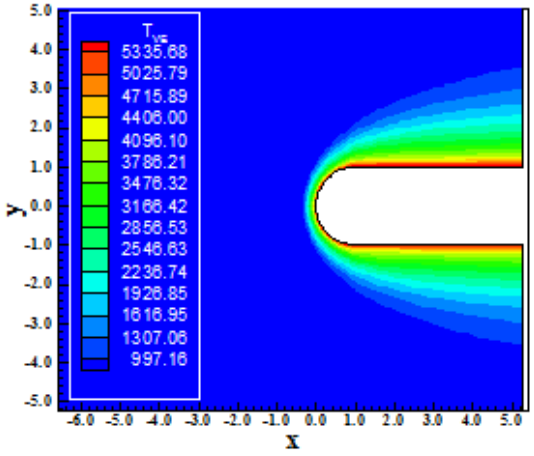

Figure 78. Vibrational temperature contours (P-LS).

Figures 79 and 80 exhibit the species mass fraction distributions along the stagnation line generated by the [2-3] schemes, respectively. Good formation of NO is detected by the numerical algorithms with the respective dissociation of the N_2 and O_2.

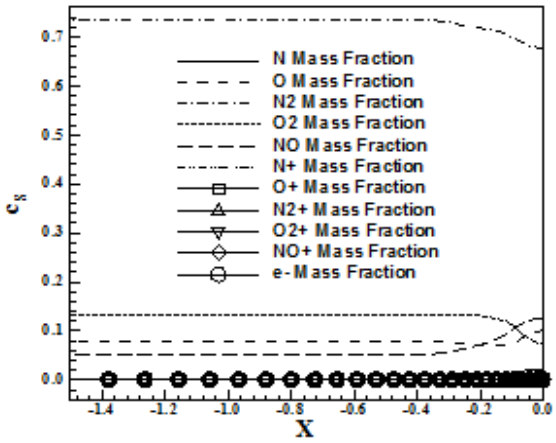

Figure 79. Species mass fraction along the stagnation line (P-VL).

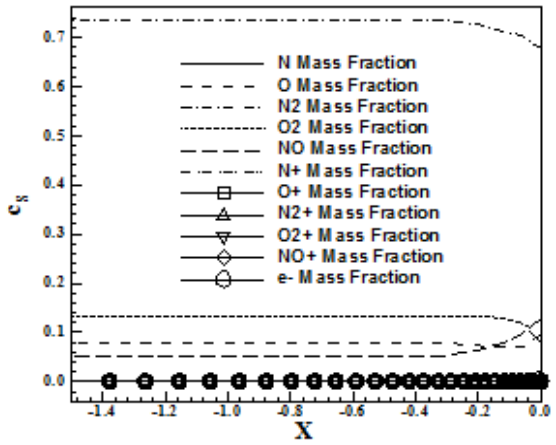

Figure 80. Species mass fraction along the stagnation line (P-LS).

2.3. Dunn and Kang complete model

2.3.1. Structured, inviscid and first-order solutions

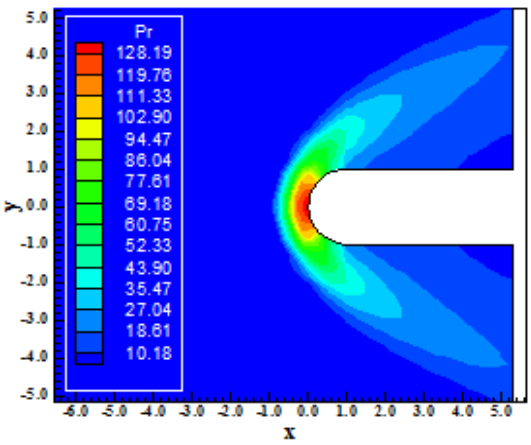

Figure 81. Pressure contours (DK-VL).

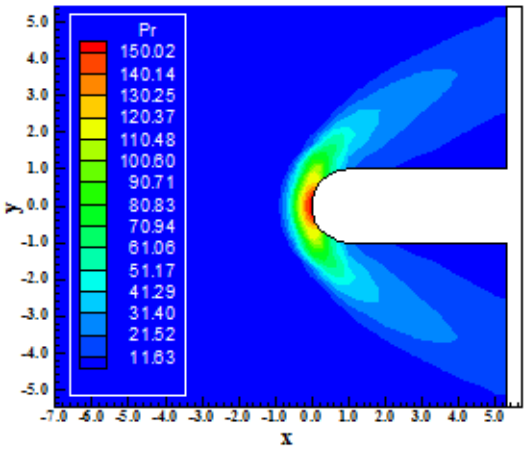

Figure 82. Pressure contours (DK-LS).

Figures 81 and 82 exhibit the pressure contours obtained by the [2] and by the [3] algorithms as using the [6] chemical model and the complete eleven species formulation. The [3] shock wave is stronger than the [2] shock wave.

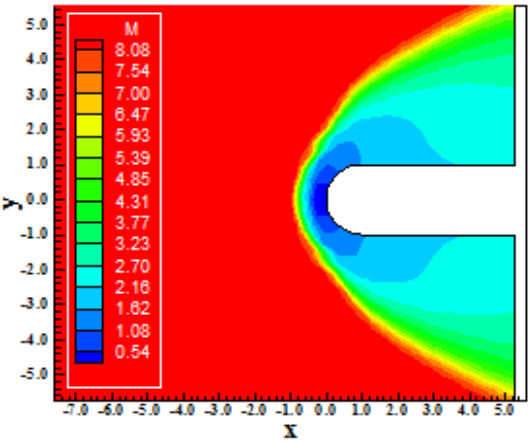

Figure 83. Mach number contours (DK-VL).

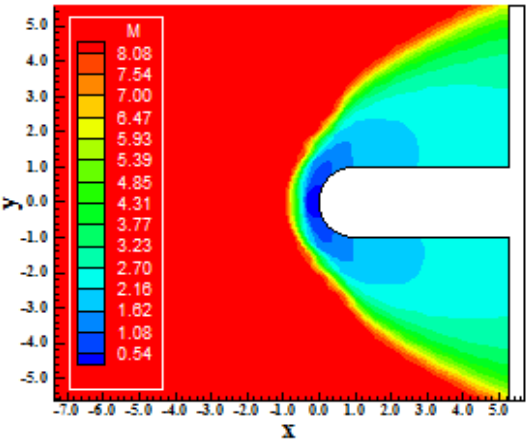

Figure 84. Mach number contours (DK-LS).

Figures 83 and 84 present the Mach number fields. The solution presented by the [2] scheme is better, qualitatively, than the [3] solution. The Mach number field presents the expected behavior.

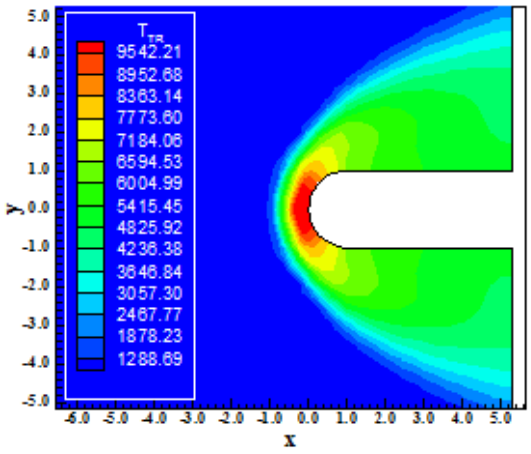

Figure 85. Translational/rotational temperature contours (DK-VL).

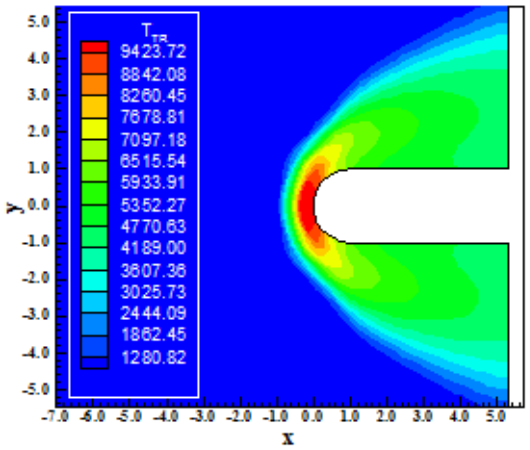

Figure 86. Translational/rotational temperature contours (DK-LS).

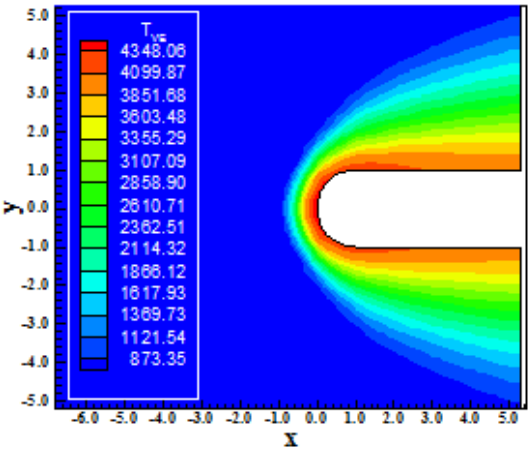

Figure 87. Vibrational temperature contours (DK-VL).

Figures 85 and 86 exhibit the translational / rotational temperature fields generated by the [2-3]

schemes, respectively. Both solutions present translational/rotational temperature peaks above 9,000 K, being the most intense due to [2]. Figures 87 and 88 show the vibrational temperature contours, whence the most intense is due to [3].

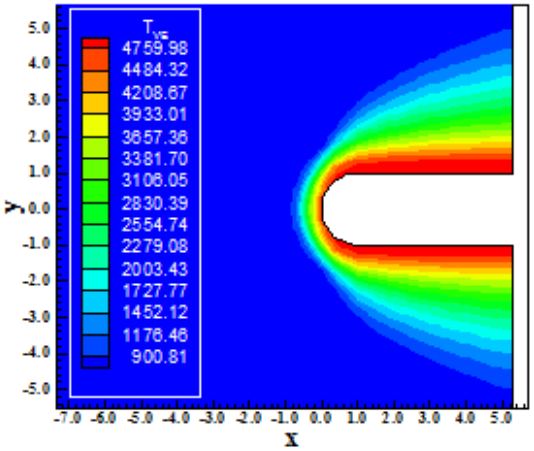

Figure 88. Vibrational temperature contours (DK-LS).

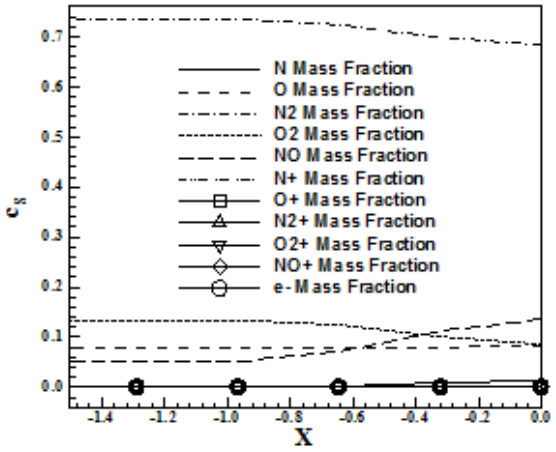

Figure 89. Species mass fraction along the stagnation line (DK-VL).

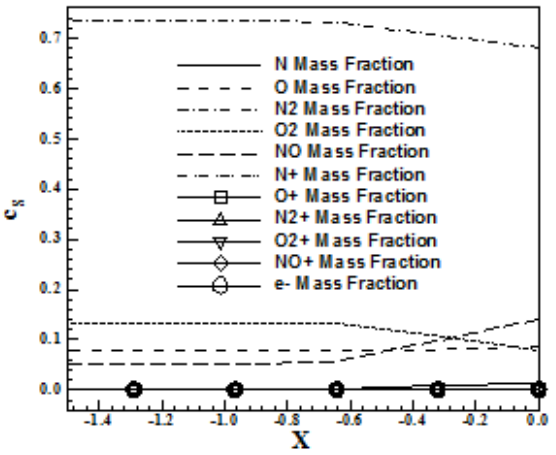

Figure 90. Species mass fraction along the stagnation line (DK-LS).

Figures 89 and 90 present the species mass fraction distributions generated by the [2-3] schemes, respectively. Both solutions present good dissociation of N_2 and O_2, with the subsequent increase in the formation of NO.

2.3.2. Structured, viscous and first-order solutions

Figures 91 and 92 show the pressure contours obtained by the [2] and by the [3] algorithms, respectively. The [2] solution presents a more severe pressure field than the [3] solution. Good symmetry properties are observed.

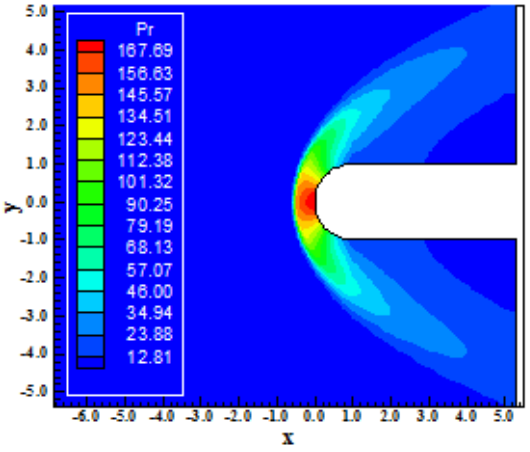

Figure 91. Pressure contours (DK-VL).

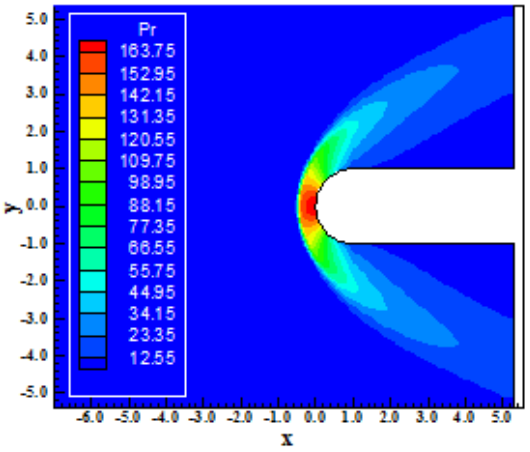

Figure 92. Pressure contours (DK-LS).

Figures 93 and 94 exhibit the Mach number field generated by the [2-3] schemes, respectively. Good qualitative aspects are observed in both figures. The boundary layer is more pronounced in the [2] solution, as well the subsonic region close to the body's surface.

Figures 95 and 96 show the translational / rotational temperature contours in the field

generated by the [2-3] algorithms, respectively. Figures 97 and 98 exhibit the vibrational temperature contours obtained by the [2] and by the [3] schemes. The [3] solutions is more intense.

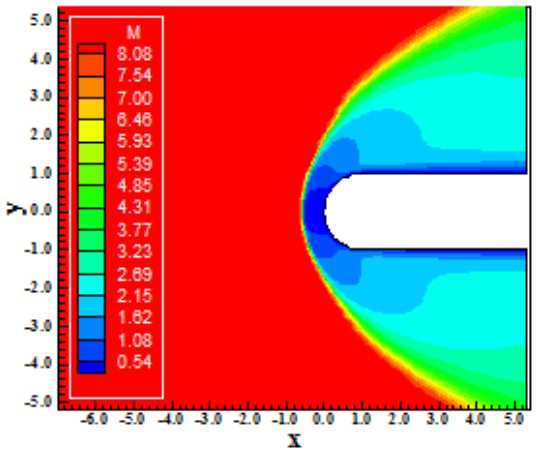

Figure 93. Mach number contours (DK-VL).

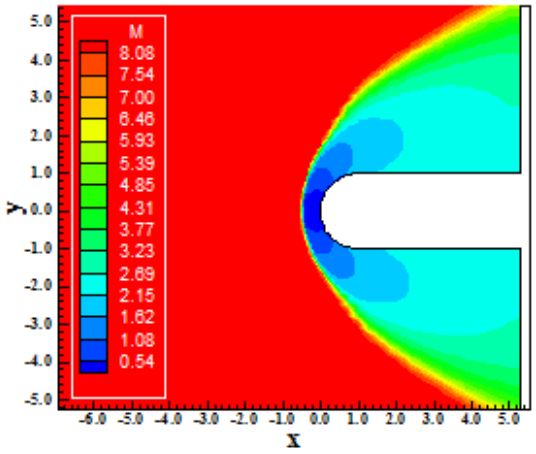

Figure 94. Mach number contours (DK-LS).

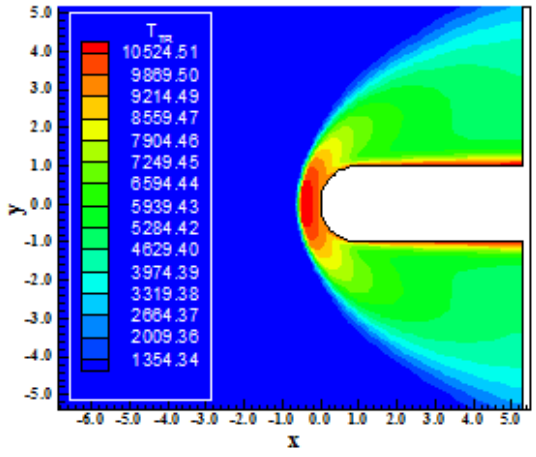

Figure 95. Translational/rotational temperature contours (DK-VL).

Figures 99 and 100 present the species mass fraction distributions along the stagnation line obtained by the [2] and by the [3] algorithms. Good formation of NO and O is observed due to the N_2 and O_2 dissociations.

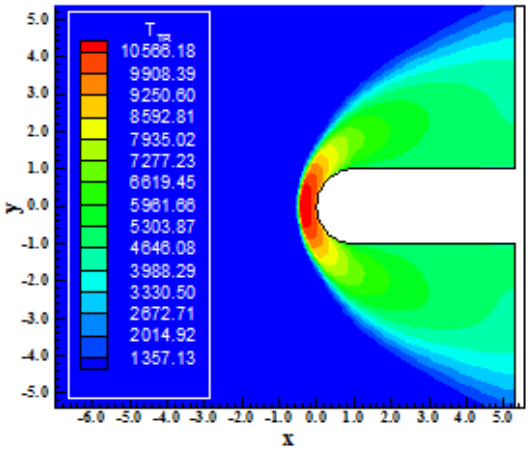

Figure 96. Translational/rotational temperature contours (DK-LS).

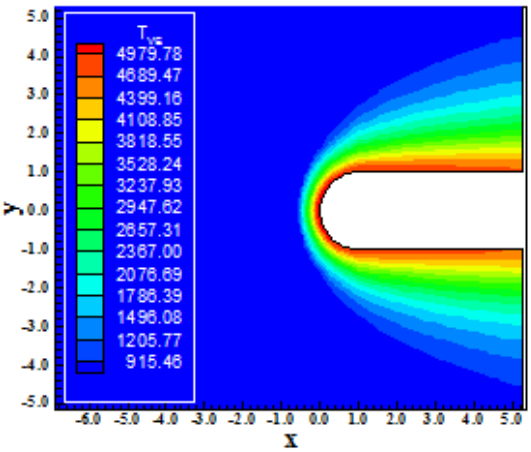

Figure 97. Vibrational temperature contours (DK-VL).

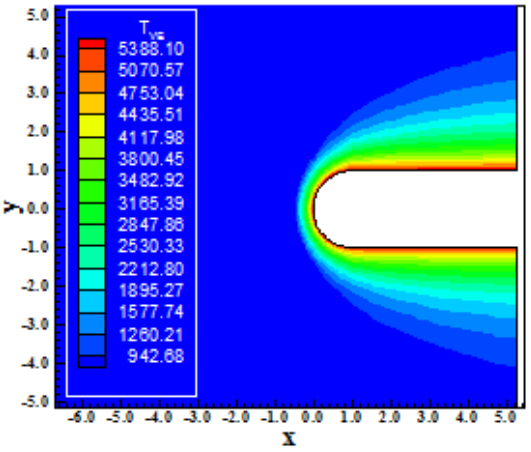

Figure 98. Vibrational temperature contours (DK-LS).

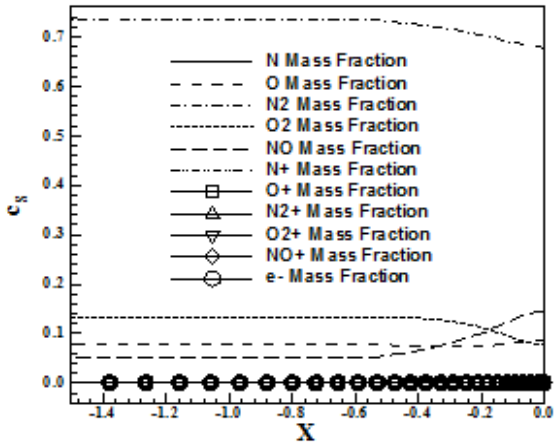

Figure 99. Species mass fraction along the stagnation line (DK-VL).

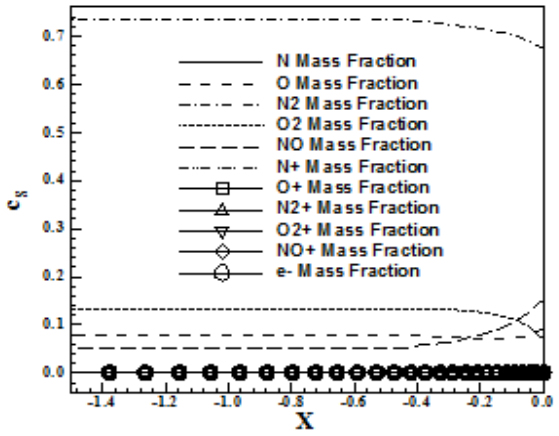

Figure 100. Species mass fraction along the stagnation line (DK-LS).

2.3.3. Structured, inviscid and second-order solutions

Figures 101 and 102 exhibit the pressure contours obtained by the [2] and by the [3] numerical schemes, respectively, in the solution of the Euler equations using the [6] chemical model and complete eleven species formulation. The [3] pressure contours are more severe.

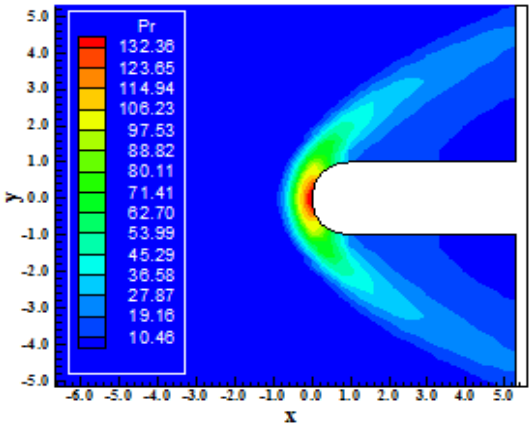

Figure 101. Pressure contours (DK-VL).

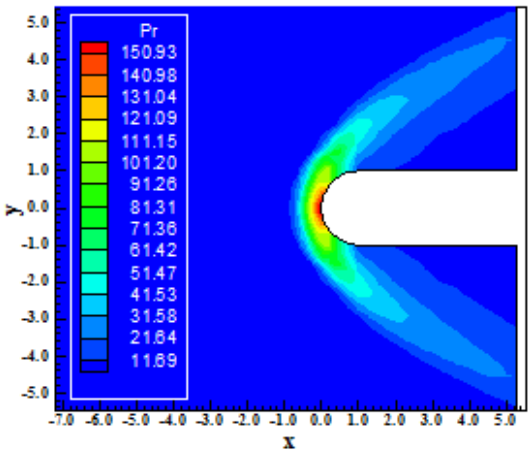

Figure 102. Pressure contours (DK-LS).

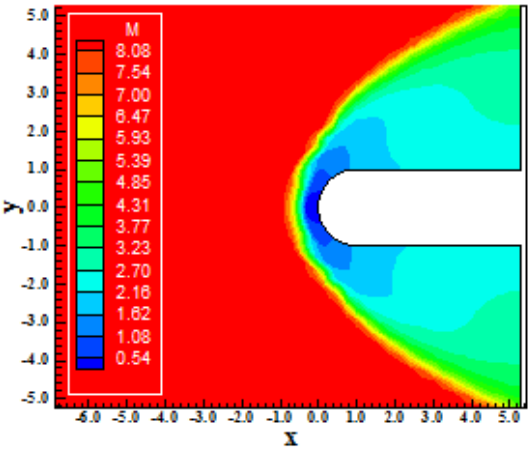

Figure 103. Mach number contours (DK-VL).

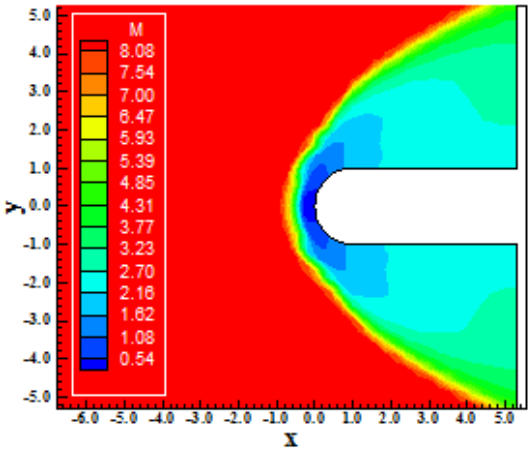

Figure 104. Mach number contours (DK-LS).

Figures 103 and 104 show the Mach number contours generated by the [2-3] algorithms, respectively. Both fields are very similar and the shock wave describes the expected behavior. The [2] solution is smoother than the [3] solution.

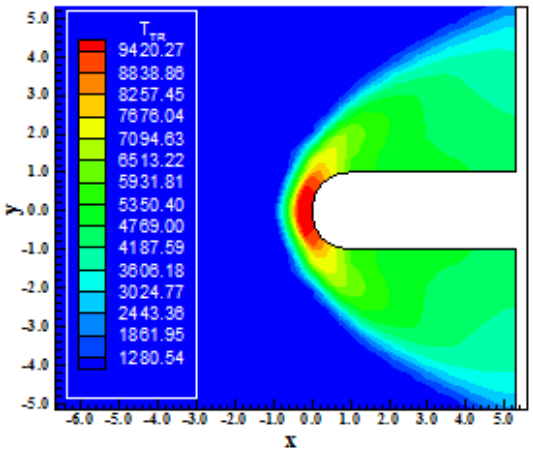

Figure 105. Translational/rotational temperature contours (DK-VL).

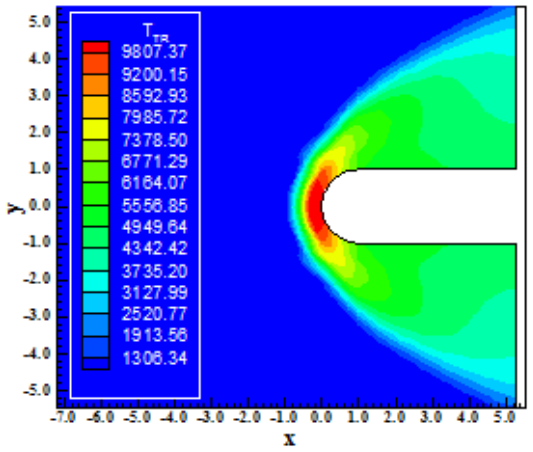

Figure 106. Translational/rotational temperature contours (DK-LS).

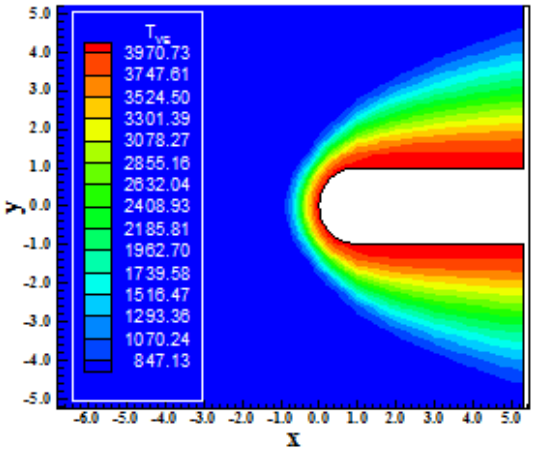

Figure 107. Vibrational temperature contours (DK-VL).

Figures 105 and 106 show the translational / rotational temperature contours obtained by the [2] and by the [3] schemes. These results are obtained with the [6] chemical model and with the complete eleven species formulation. The most intense translational/rotational temperature field is due to [3]. Figures 107 and 108 exhibit the vibrational temperature fields generated by the [2-3] schemes. The most intense is due to the [2] solution.

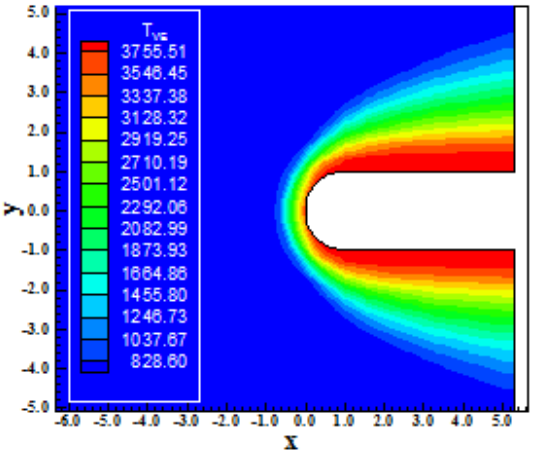

Figure 108. Vibrational temperature contours (DK-LS).

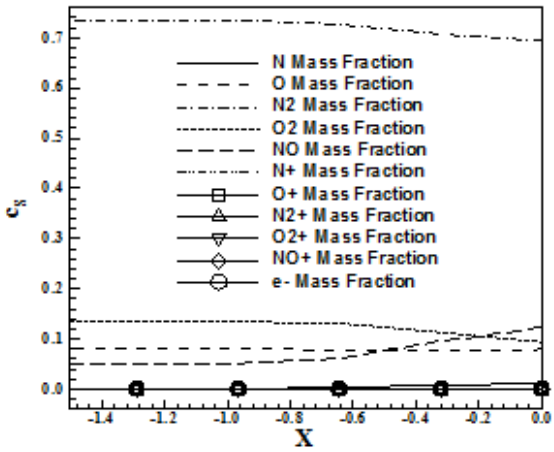

Figure 109. Species mass fraction along the stagnation line (DK-VL).

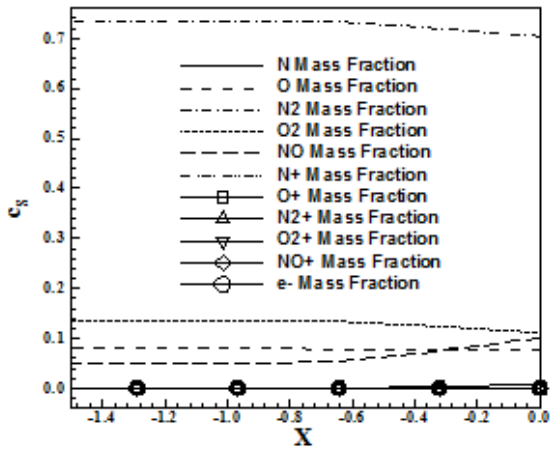

Figure 110. Species mass fraction along the stagnation line (DK-LS).

Figures 109 and 110 exhibit the species mass fraction distributions along the stagnation line generated by the [2-3] schemes. Good formation of

NO together with O is observed, in opposition to the N_2 and O_2 dissociation.

2.3.4. Structured, viscous and second-order solutions

Figures 111 and 112 present the pressure contours generated by the [2-3] schemes in the viscous and second-order formulation. Both pressure fields are very similar, but the [2] solution presents better qualitative behavior and higher pressure peak.

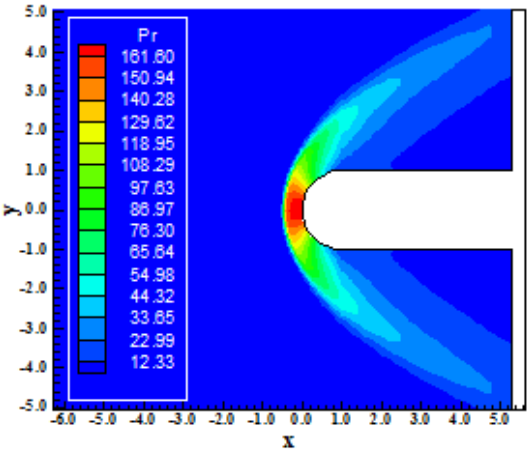

Figure 111. Pressure contours (DK-VL).

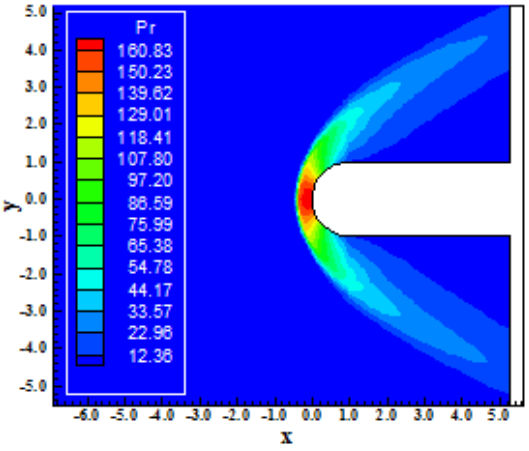

Figure 112. Pressure contours (DK-LS).

Figures 113 and 114 show the Mach number fields obtained by the [2] and by the [3] schemes. The Mach number field generated by the [2] algorithm is more intense than that generated by the [3] algorithm.

Figures 115 and 116 exhibit the translational / rotational temperature contours obtained by the [2] and by the [3] algorithms. Both solutions present temperature peaks above 10,000 K, very superior to those obtained with the incomplete model, highlighting that the complete formulation predicts more conservative temperature fields than its incomplete counterpart. Figures 117 and 118 show the vibrational temperature contours with the highest peak resulting from the [3] scheme.

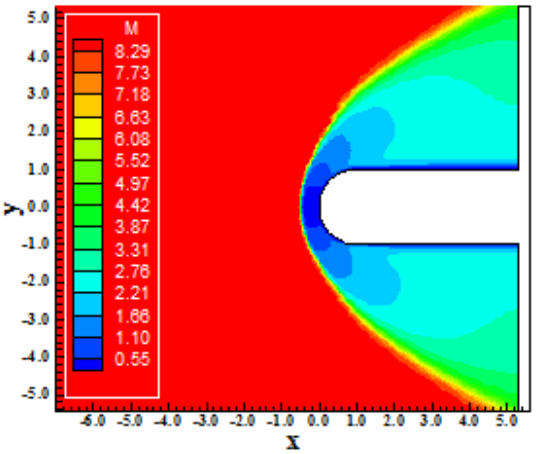

Figure 113. Mach number contours (DK-VL).

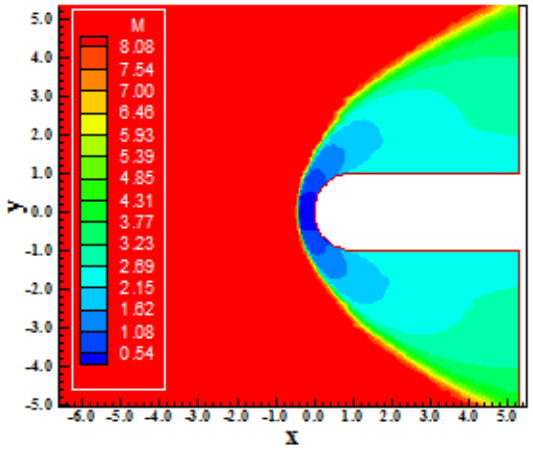

Figure 114. Mach number contours (DK-LS).

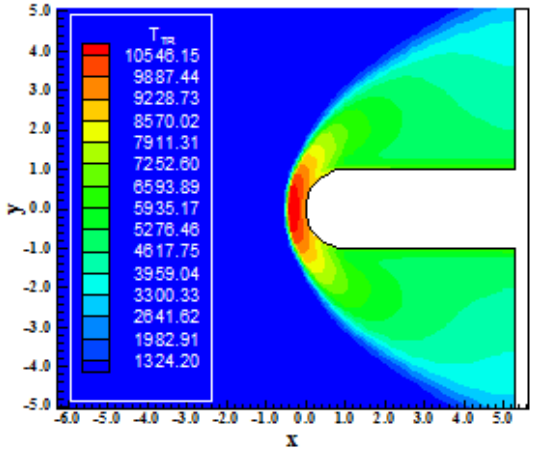

Figure 115. Translational/rotational temperature contours (DK-VL).

As seen until now, in the majority of the studied cases in this work, the [2] algorithm has produced the more severe fields and more conservative

solutions, which characterizes it as the best algorithm to predict severe conditions. In terms of solution quality, the [2] scheme is also better. Figures 119 and 120 present the species mass fraction distributions along the stagnation line obtained by the [2] and by the [3] schemes, respectively.

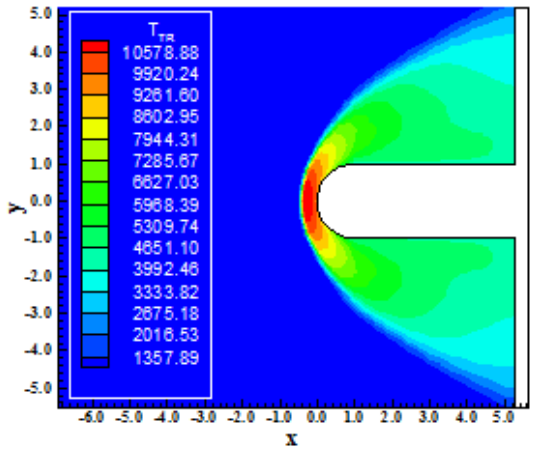

Figure 116. Translational/rotational temperature contours (DK-LS).

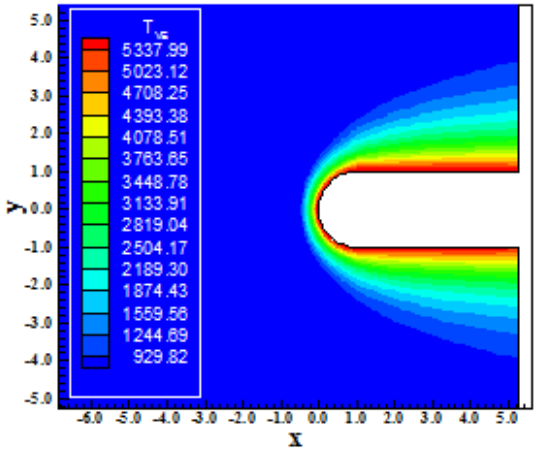

Figure 117. Vibrational temperature contours (DK-VL).

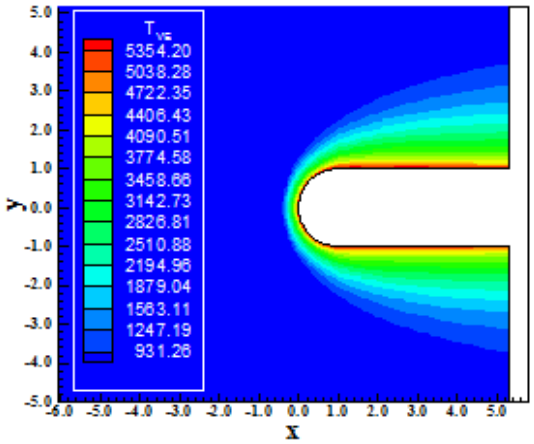

Figure 118. Vibrational temperature contours (DK-LS).

As can be seen, the NO and O formations are well captured by the [2] and [3] schemes. The dissociation of the N_2 and O_2 is also well captured.

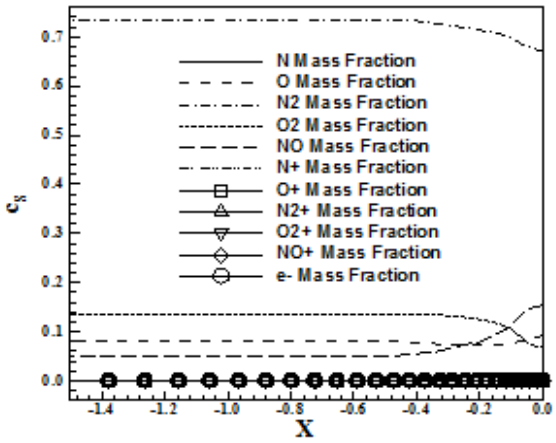

Figure 119. Species mass fraction along the stagnation line (DK-VL).

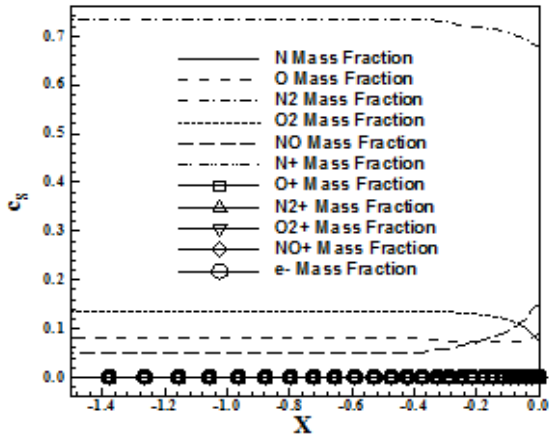

Figure 120. Species mass fraction along the stagnation line (DK-LS).

2.4. Park complete model

2.4.1. Structured, inviscid and first-order solutions

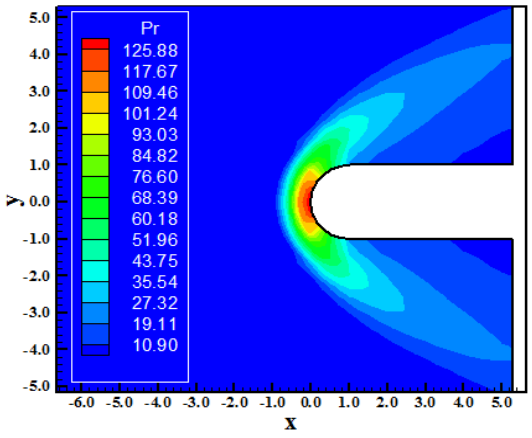

Figure 121. Pressure contours (P-VL).

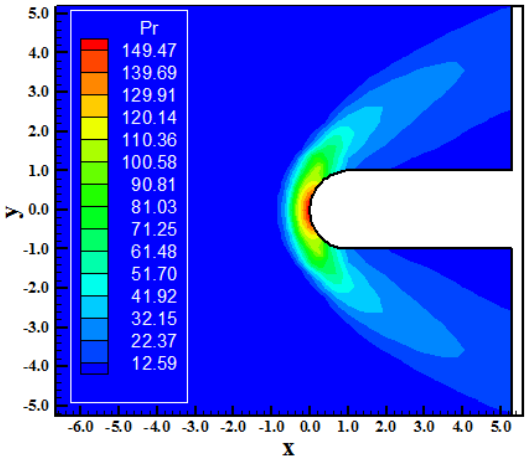

Figure 122. Pressure contours (P-LS).

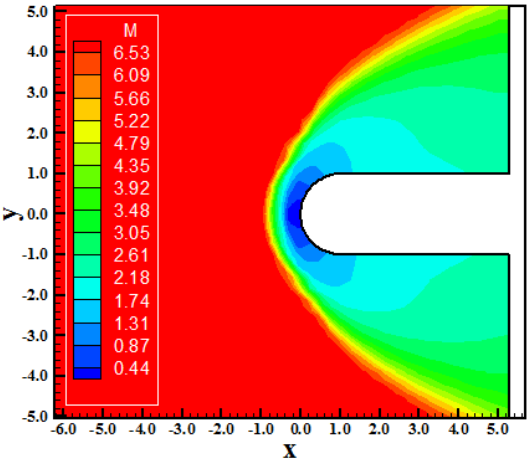

Figure 123. Mach number contours (P-VL).

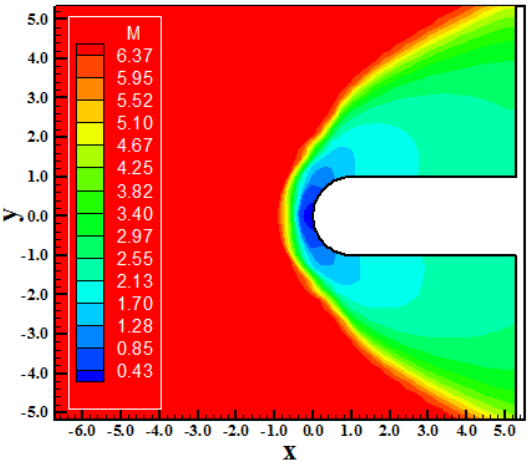

Figure 124. Mach number contours (P-LS).

Figures 121 and 122 exhibit the pressure contours generated by the [2-3] numerical schemes, respectively. The most severe pressure field is obtained by the [3] solution. Figures 123 and 124 show the Mach number field obtained by the [2] and by the [3] numerical algorithms, respectively. The most severe Mach number field is that obtained by the [2] scheme. Figures 125 and 126 present the translational/rotational temperature contours obtained by the [2] and by the [3] algorithms.

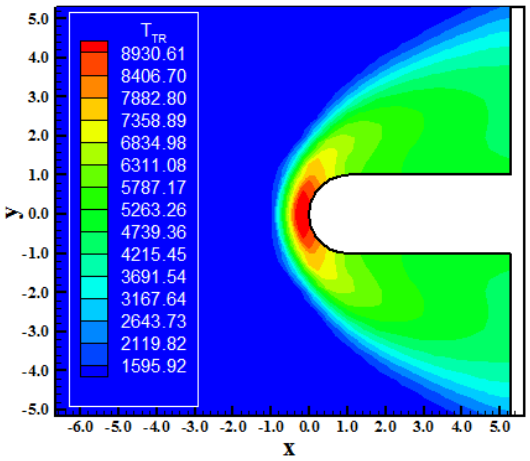

Figure 125. Translational/rotational temperature contours (P-VL).

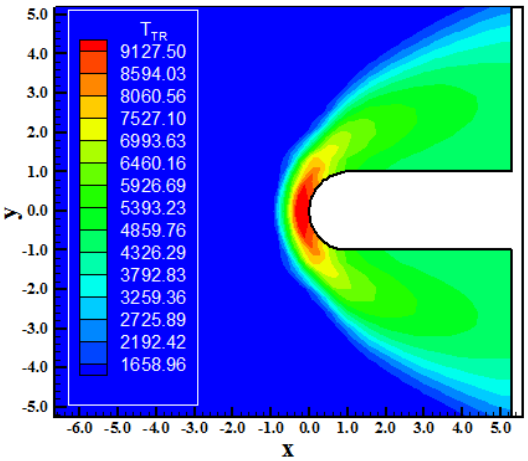

Figure 126. Translational/rotational temperature contours (P-LS).

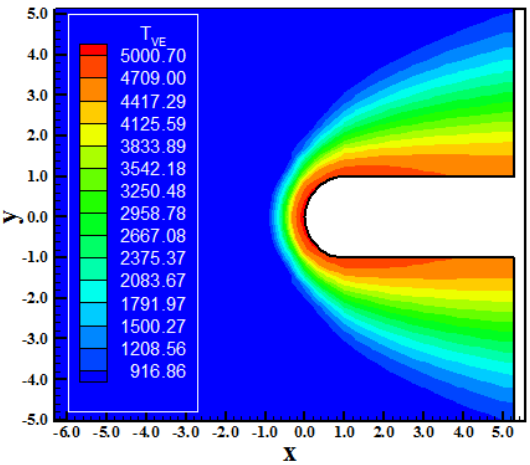

Figure 127. Vibrational temperature contours (P-VL).

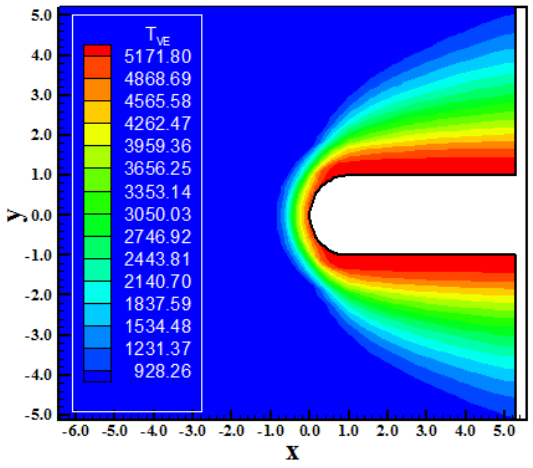

Figure 128. Vibrational temperature contours (P-LS).

The most severe translational/rotational temperature field is due to [3]. Figures 127 and 128 exhibit the vibrational temperature contours obtained by [2-3]. The most intense vibrational temperature field is due to [3]. Figures 129 and 130 present the species mass fraction distributions generated by [2-3].

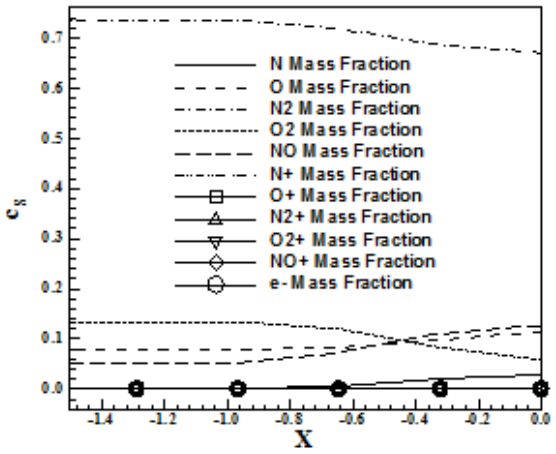

Figure 129. Species mass fraction along the stagnation line (P-VL).

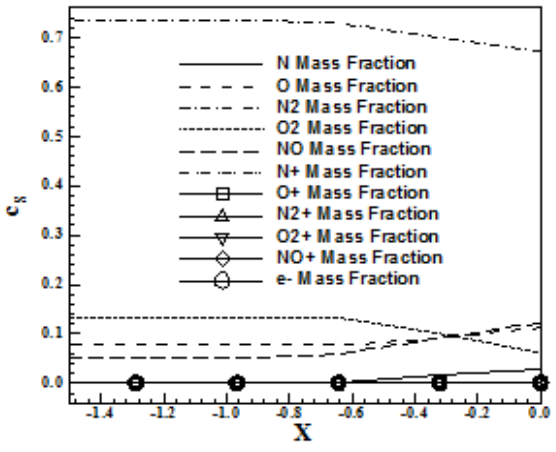

Figure 130. Species mass fraction along the stagnation line (P-LS).

Both solutions present good formation of NO and O, due to the good dissociation of N_2 and O_2.

2.4.2. Structured, viscous and first-order solutions

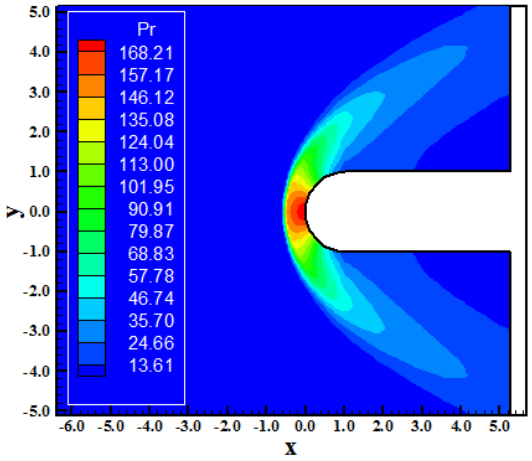

Figure 131. Pressure contours (P-VL).

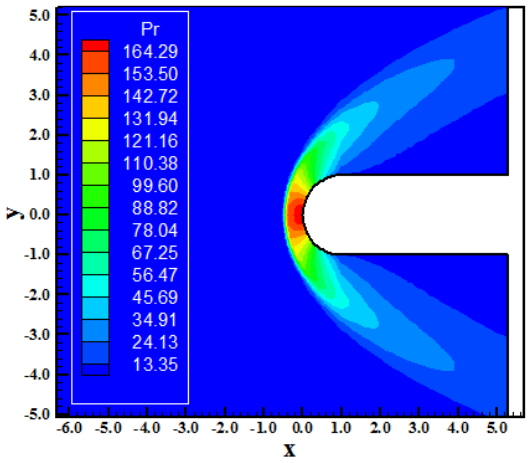

Figure 132. Pressure contours (P-LS).

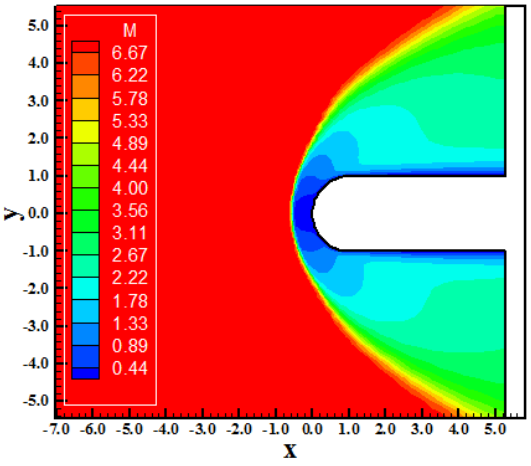

Figure 133. Mach number contours (P-VL).

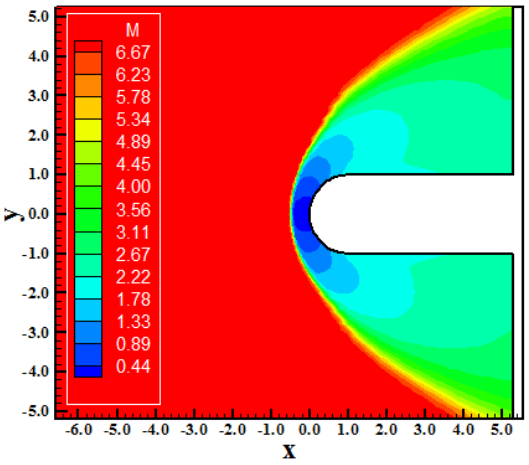

Figure 134. Mach number contours (P-LS).

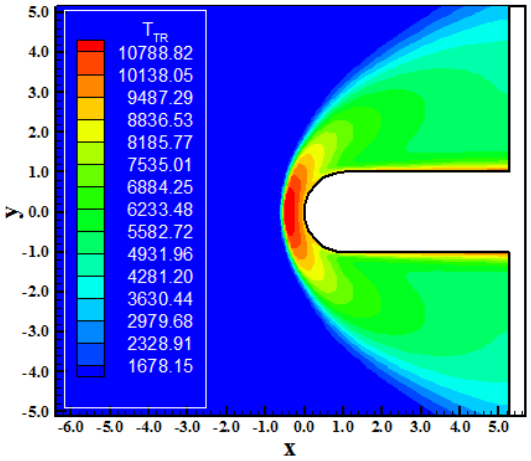

Figure 135. Translational/rotational temperature contours (P-VL).

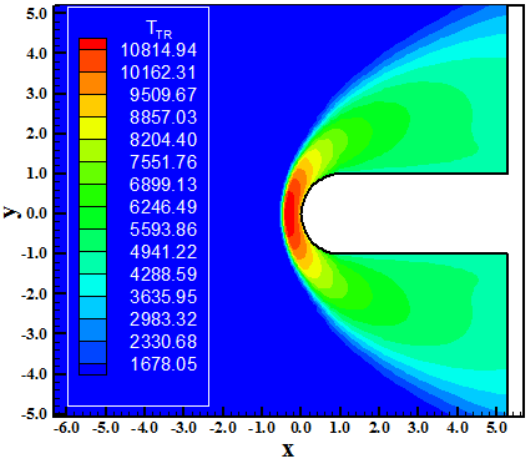

Figure 136. Translational/rotational temperature contours (P-LS).

Figures 131 and 132 exhibit the pressure contours obtained by [2] and by [3] schemes. The most severe pressure field is due to [2]. Figures 133 and 134 show the Mach number fields generated by [2] and by [3]. Both solutions don't present meaningful differences. Figures 135 and 136 present the translational/rotational temperature contours obtained by the [2-3] algorithms. The most intense temperature field is due to [3]. Temperatures above 10,500 K are reached.

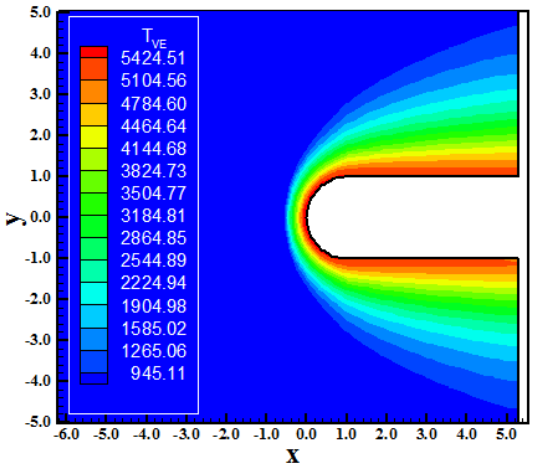

Figure 137. Vibrational temperature contours (P-VL).

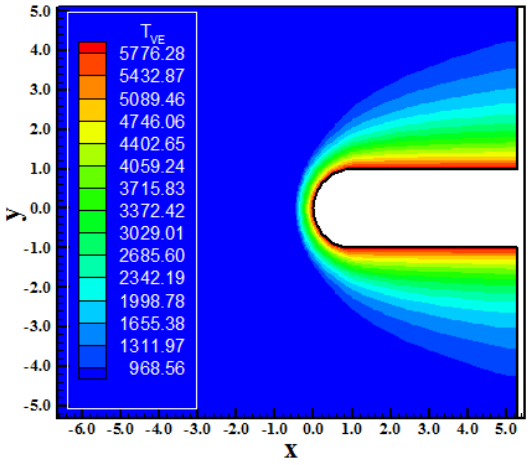

Figure 138. Vibrational temperature contours (P-LS).

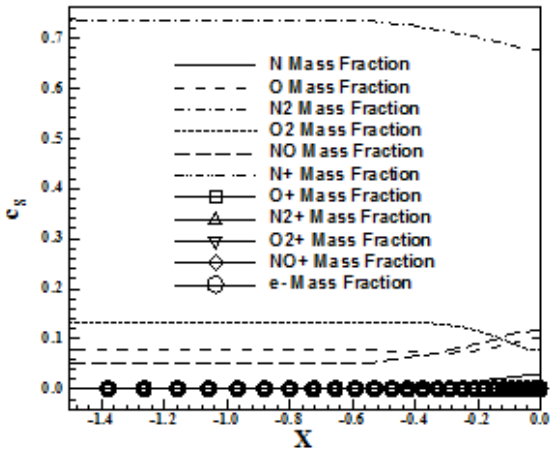

Figure 139. Species mass fraction along the stagnation line (P-VL).

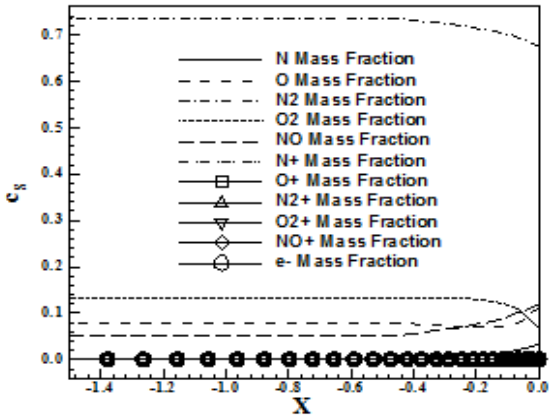

Figure 140. Species mass fraction along the stagnation line (P-LS).

Figures 137 and 138 exhibit the vibrational temperature contours obtained by the [2-3] schemes. The most intense is due to [3]. Finally, Figures 139 and 140 show the species mass fraction distributions generated by the [2-3] schemes. Both solutions present good formation of NO and O.

2.4.3. Structured, inviscid and second-order solutions

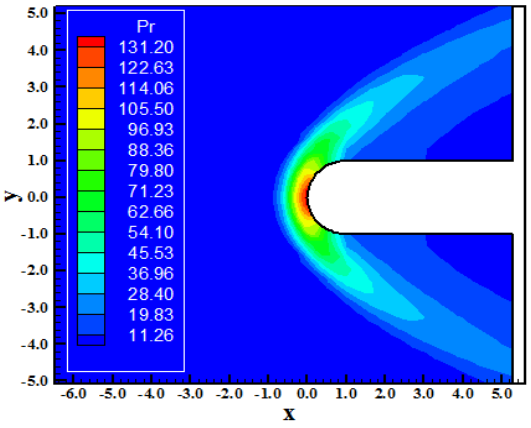

Figure 141. Pressure contours (P-VL).

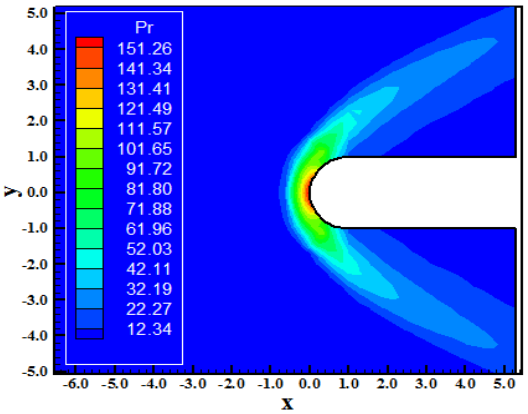

Figure 142. Pressure contours (P-LS).

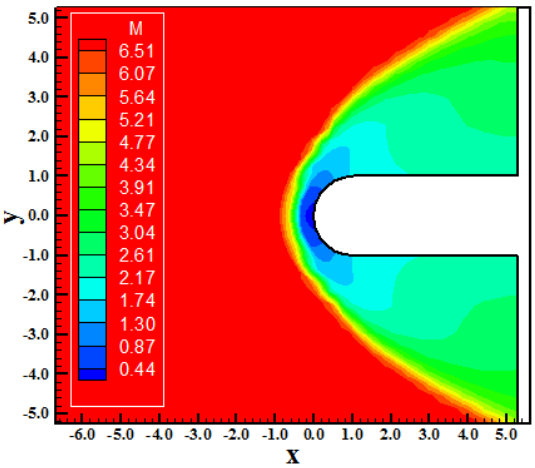

Figure 143. Mach number contours (P-VL).

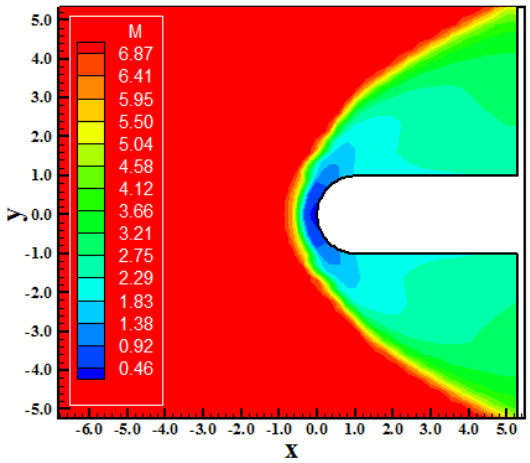

Figure 144. Mach number contours (P-LS).

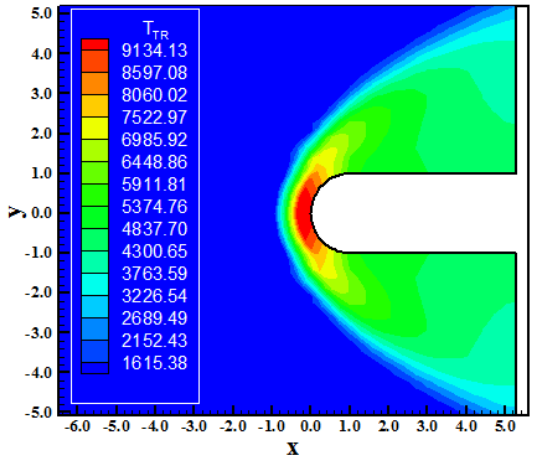

Figure 145. Translational/rotational temperature contours (P-VL).

Figures 141 and 142 exhibit the pressure contours obtained by [2] and by [3], respectively. The most severe pressure field is due to [3]. Figures 143 and 144 show the Mach number fields

generated by [2] and by [3]. The most intense Mach number field is due to [3]. Figures 145 and 146 show the translational/rotational temperature contours generated by [2-3]. The most intense temperature field is due to [2]. Figures 147 and 148 present the vibrational temperature contours.

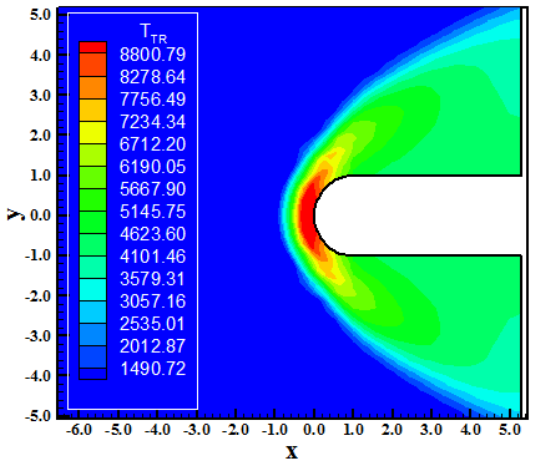

Figure 146. Translational/rotational temperature contours (P-LS).

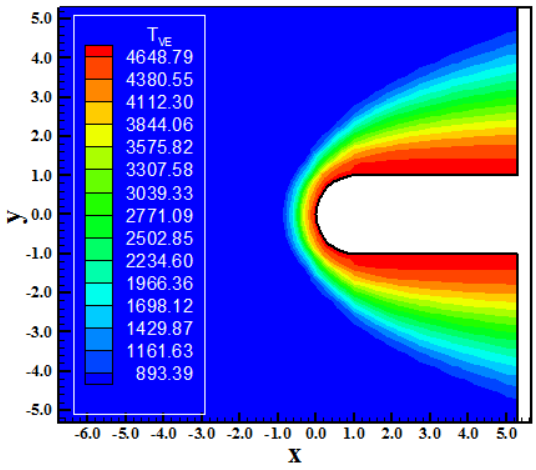

Figure 147. Vibrational temperature contours (P-VL).

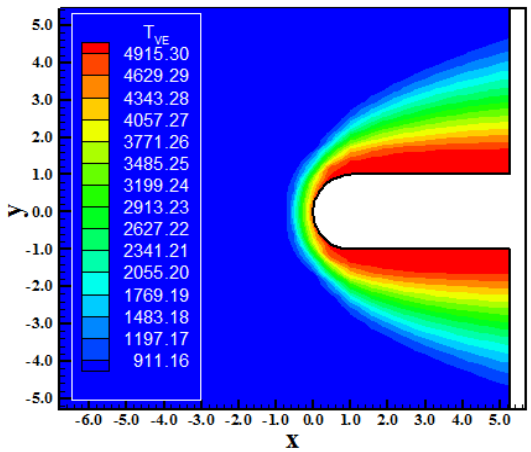

Figure 148. Vibrational temperature contours (P-LS).

The most intense vibrational field is due to [3]. Finally, Figures 149 and 150 exhibits the species mass fraction distributions along the stagnation line obtained by [2-3]. Good formation of NO, O and N, due to the N_2 and O_2 dissociations.

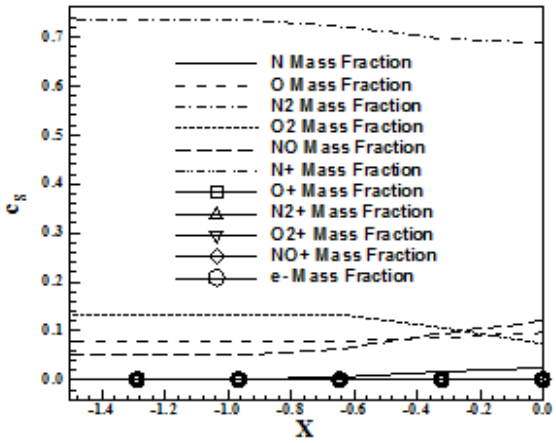

Figure 149. Species mass fraction along the stagnation line (P-VL).

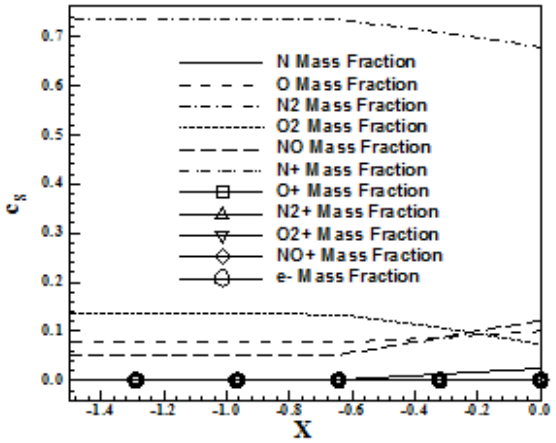

Figure 150. Species mass fraction along the stagnation line (P-LS).

2.4.4. Structured, viscous and second-order solutions

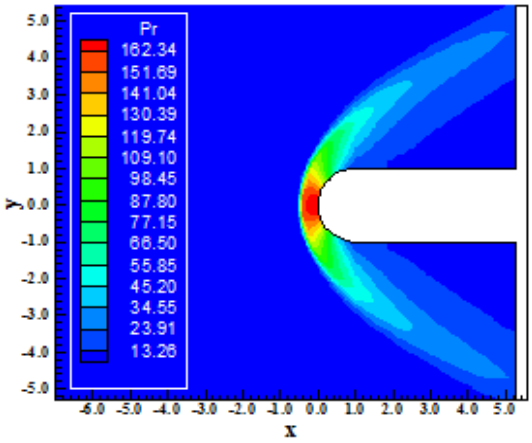

Figure 151. Pressure contours (P-VL).

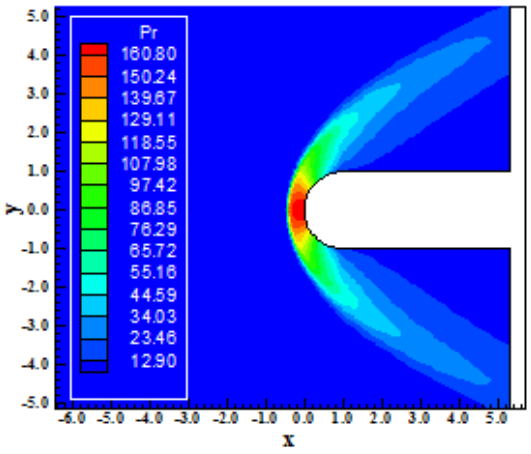

Figure 152. Pressure contours (P-LS).

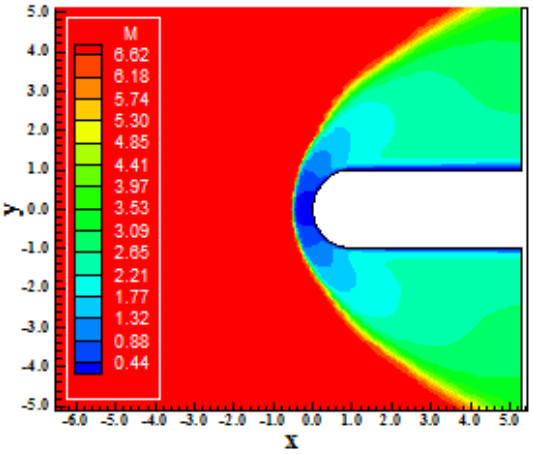

Figure 153. Mach number contours (P-VL).

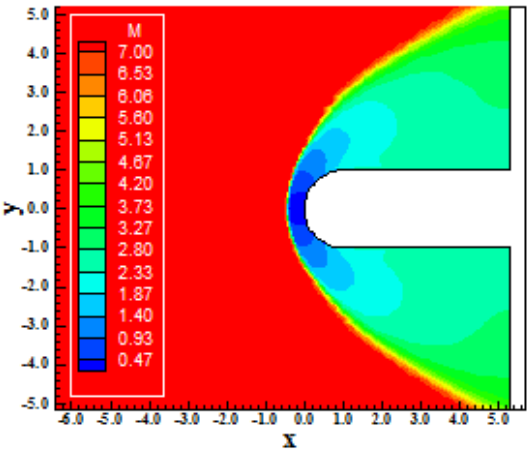

Figure 154. Mach number contours (P-LS).

Figures 151 and 152 exhibit the pressure contours obtained by the [2] and by the [3] schemes. The most severe is due to [2]. Figures 153 and 154 show the Mach number fields generated by the [2-3] schemes. The most intense Mach number field is due to [3]. Figures 155 and 156 present the translational/rotational temperature field, in which the most severe field is due to [3]. Figures 157 and 158 exhibit the vibrational temperature fields generated by [2-3]. The most intense field is due to [2]. Finally, Figures 159 and 160 show the species mass fraction distributions generated by [2-3]. Good NO and O formations are observed.

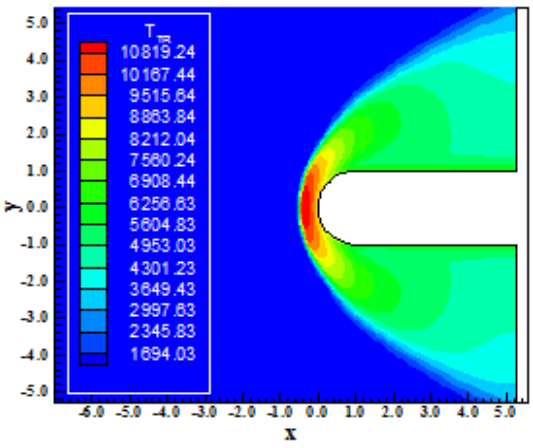

Figure 155. Translational/rotational temperature contours (P-VL).

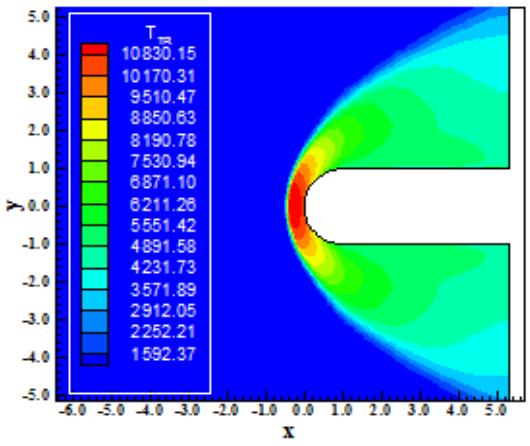

Figure 156. Translational/rotational temperature contours (P-LS).

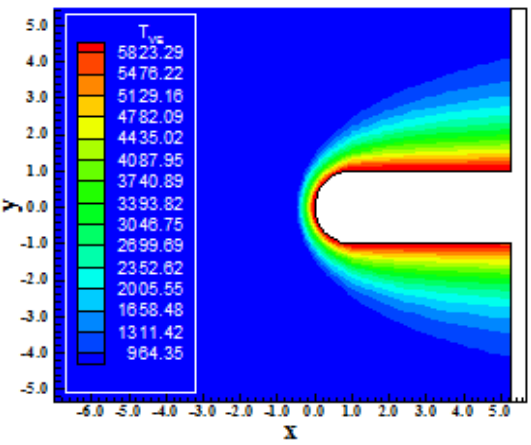

Figure 157. Vibrational temperature contours (P-VL).

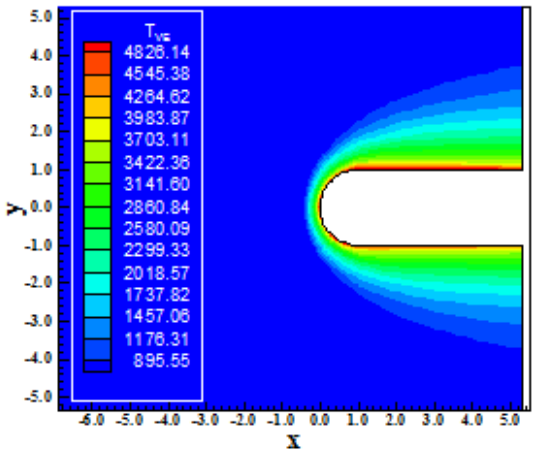

Figure 158. Vibrationa temperature contours (P-LS).

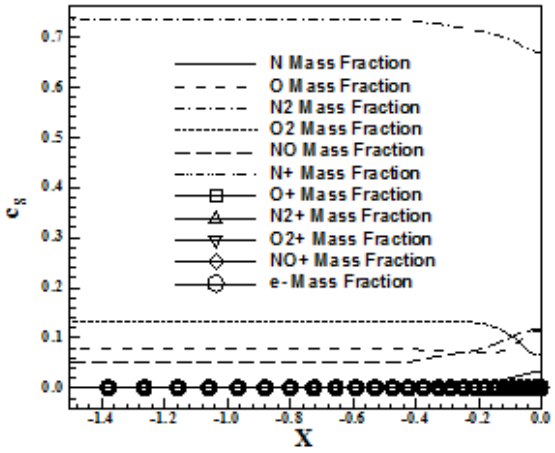

Figure 159. Species mass fraction along the stagnation line (P-VL).

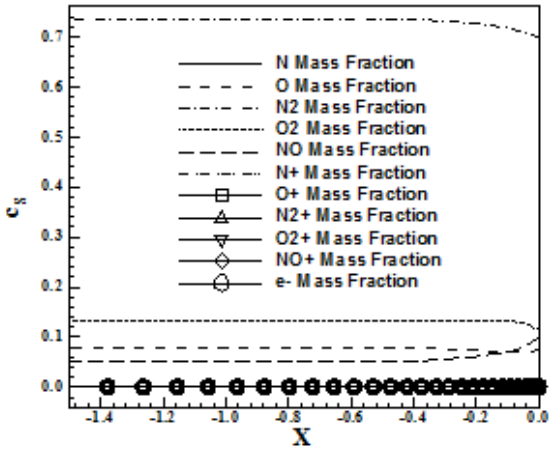

Figure 160. Species mass fraction along the stagnation line (P-LS).

3 Conclusion

This work, second of this study, describes a numerical tool to perform thermochemical non-equilibrium simulations of reactive flow in two-dimensions, using an eleven species chemical model. The [2-3] schemes, in their first- and second-order versions, are implemented to accomplish the numerical simulations. The Euler and Navier-Stokes equations, on a finite volume context and employing structured and unstructured spatial discretizations, are applied to solve the "hot gas" hypersonic flows around a blunt body, around a double ellipse, and around a reentry capsule in two-dimensions. The second-order versions of the [2-3] schemes are obtained from a "MUSCL" extrapolation procedure in a context of structured spatial discretization. In terms of unstructured spatial discretization, only first-order solutions are presented.

The results have shown that the [2] algorithm yields smoother solutions than the [3] algorithm, characterizing the form as providing better qualitative solutions, appropriated to a more refined phase of airplane project. Moreover, the [2] scheme yields more severe solutions, characterizing again the former as more conservative and appropriated to initial phases of project of airplanes.

References:

[1] E. S. G. Maciel, and A. P., Pimenta, Thermochemical Non-Equilibrium Reentry Flows in Two-Dimensions – Eleven Species Model – Part I, *Wseas Transactions on Applied and Theoretical Mechanics* (under review)

[2] B. Van Leer, Flux-Vector Splitting for the Euler Equations, *Lecture Notes in Physics*, Springer Verlag, Berlin, Vol. 170, pp. 507-512, 1982.

[3] M. Liou, and C. J. Steffen Jr., A New Flux Splitting Scheme, *Journal of Computational Physics*, Vol. 107, 1993, pp. 23-39.

[4] E. S. G. Maciel, Analysis of Convergence Acceleration Techniques Used in Unstructured Algorithms in the Solution of Aeronautical Problems – Part I, *Proceedings of the XVIII International Congress of Mechanical Engineering (XVIII COBEM)*, Ouro Preto, MG, Brazil, 2005. [CD-ROM]

[5] E. S. G. Maciel, Analysis of Convergence Acceleration Techniques Used in Unstructured Algorithms in the Solution of Aerospace Problems – Part II, *Proceedings of the XII Brazilian Congress of Thermal Engineering and Sciences (XII ENCIT)*, Belo Horizonte, MG, Brazil, 2008. [CD-ROM]

[6] M. G. Dunn, and S. W. Kang, Theoretical and Experimental Studies of Reentry Plasmas, *NASA CR-2232*, 1973.

[7] C. Park, Assessment of Two-Temperature Kinetic Model for Ionizing Air, *Journal of Thermophysics and Heat Transfer*, Vol. 3, No. 13, pp. 233-244, 1989.